Multiple growths of high-entropy alloy nanostructures for energy conversion

Du, Tri Quang

2023

Du, T. Q. (2023). Multiple growths of high-entropy alloy nanostructures for energy conversion. Master's thesis, Nanyang Technological University, Singapore. https://hdl.handle.net/10356/169176

https://hdl.handle.net/10356/169176

https://doi.org/10.32657/10356/169176

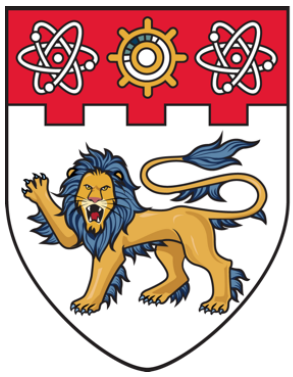

NANYANG TECHNOLOGICAL UNIVERSITY
SINGAPORE

MULTIPLE GROWTHS OF HIGH-ENTROPY ALLOY NANOSTRUCTURES FOR ENERGY CONVERSION

DU TRI QUANG

SCHOOL OF MATERIALS SCIENCE AND ENGINEERING

2023

MULTIPLE GROWTHS OF HIGH-ENTROPY ALLOY NANOSTRUCTURES FOR ENERGY CONVERSION

DU TRI QUANG

SCHOOL OF MATERIALS SCIENCE AND ENGINEERING

A thesis submitted to the Nanyang Technological University
in partial fulfilment of the requirement for the degree of
Master of Engineering

2023

Statement of Originality

I hereby certify that the work embodied in this thesis is the result of original research, is free of plagiarised materials, and has not been submitted for a higher degree to any other University or Institution.

14/02/2023

. . . . . .

Date

. . . . . .

DU TRI QUANG

Supervisor Declaration Statement

I have reviewed the content and presentation style of this thesis and declare it is free of plagiarism and of sufficient grammatical clarity to be examined. To the best of my knowledge, the research and writing are those of the candidate except as acknowledged in the Author Attribution Statement. I confirm that the investigations were conducted in accord with the ethics policies and integrity standards of Nanyang Technological University and that the research data are presented honestly and without prejudice.

14/02/2023

. . . . . .

Date

. . . . . .

Assoc. Prof. HUANG YIZHONG

Authorship Attribution Statement

This thesis **does not** contain any materials from papers published in peer-reviewed journals or from papers accepted at conferences in which I am listed as an author.

14/02/2023

. . . . . .
Date

. . . . . .
DU TRI QUANG

Abstract

The energy predicament and environmental issues are the foremost challenges to mankind, drawing the world's attention to develop renewable and sustainable energy sources with follow-up technologies, which can convert and store clean energy sources hydro power, wind power, or solar energy into fuel cells, advanced batteries, and solar cells. One of the most promising technologies is water splitting to generate green hydrogen fuels by electricity from renewable energy sources to make a complete cycle of clean energy. The emergence of renewable energy has gained significant interest in not only developing more potential functional materials but also the fabrication of advanced catalysts that meet the affordability and stability requirements for conventional energy conversion and storage. High-entropy materials have come into sight of academic literature, escalating their understanding and applications over a broad range of applications including aerospace mechanical and structures, anti-corrosion, thermodynamic protection, and especially electrocatalysis for renewable energy. New catalyst materials can be engineered to have the higher surface area and unique crystal structure by composing multiple elements from abundant and low-cost transition metals to form non-precious metal high-entropy alloys (HEAs) and reduce the production cost to commercialize the plentiful and powerful resources of hydropower.

This research reports a rapid, shape-designable, and scalable strategy to synthesize HEA electrocatalysts, by laser irradiating of the precursor metal-salt solutions loaded on the carbon fiber paper. The near-infrared (1064 nm) laser is tunable between continuous and pulsed modes to provide not only HEA nanoparticles fabrication but also post-synthesis treatment. Multiple growths of HEA nanostructures by combining both laser irradiation modes, resulting in porous nanostructures embedded with defect-rich HEA nanoparticles. These structures enlarge the surface area and expose more active sites on the surface to boost the electrocatalytic performance. This work investigated oxygen evolution reaction (OER) of a remarkable electrocatalyst, made of multiple growths of CoCuFeMnNi high-entropy alloys on the carbon-fiber-paper substrate, served as a working electrode that can achieve 10 $mAcm^{-2}$ with 277 mV of overpotential in 1 M KOH electrolyte for OER and

remained stable functioning after over 12 hours. The formation of oxides, oxyhydroxides intermediates with synergetic surface metal active sites is predicted to escalate the oxygen evolution reaction.

This research promotes an adaptable method for the cost-effective and efficient fabrication of high-entropy alloys to enhance water splitting and further energy conversion applications.

Lay Summary

The increasing greenhouse gas emission produced by burning fossil fuels currently accounts for approximately 95 percent of global energy consumption These emissions have been the reason of several environmental challenges, especially global warming and climate change. Nevertheless, as the world approaches the technology and informatic era, the energy demand is projected to be doubled by 2050, making the search for sustainable energy solutions more urgent. The energy predicament and environmental issues are the foremost challenges to mankind. In the past few years, leading researchers have focused on developing renewable and sustainable energy sources with follow-up technologies, which can convert and store clean energy sources hydropower, wind power, or solar energy into fuel cells, advanced batteries, and solar cells. One of the most promising technologies is water splitting to generate the green hydrogen fuels by electricity from renewable energy sources, which makes a cycle of clean energy. Hydrogen evolution reaction, releasing hydrogen gas and oxygen evolution reaction, generating oxygen gas, are the two half-reactions occurring in water splitting. Electrocatalysts are essential materials that can speed up the process and increase conversion efficiency. Finding a way to lower the production cost by engineering new materials is the best path to commercialize the plentiful and powerful resources of water.

Despite the efficiency and performance of the novel energy technologies that have improved, there is still a gap to meet the cost-effective and continuous power supply requirements The use of traditional catalyst materials, such as platinum and other precious metal, can be expensive and limited in certain processes. The need for novel catalyst materials that are cost-effective and have improved performance is essential. High-entropy alloys (HEAs) are multicomponent materials that contain five or more elements in near-equimolar proportions and unique properties, which have been reported for energy-related applications. New catalyst materials can be engineered to have a higher surface area and unique crystal structure by composing HEAs from abundant and low-cost transition metals, such as iron, cobalt, nickel, copper, etc. The applications of HEA for catalysis or energy storage and conversion have been investigated for less than a decade, which lead to lots of

explorations and optimizations that are necessary for future conventional prospects.

This research provides an approach to the synthesis of non-noble metal HEAs, together with surface modification of the HEA electrocatalysts, by laser irradiation method, to achieve advanced catalytic performance. The technique based on laser irradiation is fast, shape-designable, and scale-able for industrial applications. Post-synthesis treatment by laser irradiation itself is shown to have a contribution to the formation of defects on the HEAs crystal lattice and increase the surface area for improving oxygen evolution reaction efficiency. Multiple growths of HEAs by combining the growth and treatment process in this research suggests a promising application in 3D printing HEAs electrocatalysts.

Acknowledgements

This thesis would not have been possible without the scholarship from Vingroup and NTU Graduate College (Vingroup-NTU Graduate Scholarship).

I would like to express my deepest gratitude to my research supervisor, Associate Professor Huang Yizhong, for his incisive recommendations concerning the scope of the research as well as patient guidance and encouragement. He always provides valuable suggestions, ample resources to conduct our research works and offers a dynamic atmosphere to all team members.

I would like to thank Dr. Liu Weiling, Dr. Derrick Ang, and other technicians from Facility for Analysis, Characterisation, Testing and Simulation (FACTS) for their kind training in XRD and SEM and the preservation to the equipment for systematic and comfortable use.

I would like to extend my thankfulness to my research group members: Dr. Lu Yu for his kind instruction on lab equipment, insightful discussion, and suggestion on material processing; Mr. Xiu Mingzhen for helping me with the HRTEM characterization; Mr. Wang Zheng and Mr. Wang Yong for their help in lab management and experiments.

I am most grateful to my family members for their endless love and encouragement, despite the distance from hometown and the world pandemic over these years.

Table of Contents

Table Captions

Figure Captions

Abbreviations

2D	Two-dimensional
3D	Three-dimensional
ADF	Annular Dark-field
BE	Backscattered Electron
BF	Bright-field
CC	Carbon Cloth
CFP	Carbon Fiber Paper
CNT	Carbon Nanotube
CP	Carbon Paper
CV	Cyclic Voltammetry
DFT	Density Function Theory
EDS	Energy Dispersive X-ray Spectroscopy
EIS	Electrochemical Impedance Spectroscopy
FCC	Face-centered Cubic
FESEM	Field Emission Scanning Electron Microscopy
FFT	Fast Fourier Transform
FTO	Fluorine-doped Tin Oxide
GC	Glassy Carbon
HAADF	High Angle Annular Dark-field
HEAs	High-entropy Alloys
HEMs	High-entropy Materials
HEOs	High-entropy Oxides
HER	Hydrogen Evolution Reaction
HRTEM	High Resolution Transmission Electron Microscopy
IFFT	Inverse Fast Fourier Transform
LSV	Linear Sweep Voltammetry
LT	Laser Treatment
MG	Multiple Growth
NP	Nanoparticle

NW	Nanowire
OER	Oxygen Evolution Reaction
ORR	Oxygen Reduction Reaction
PTC	Particle
RHE	Reversible Hydrogen Electrode
SEM	Scanning Electron Microscopy
SE	Secondary Electron
SG	Single Growth
SRC	Simple Randle Cell
STEM	Scanning Transmission Electron Microscopy
TEM	Transmission Electron Microscopy
XPS	X-ray Photoelectron Spectroscopy
XRD	X-ray Diffraction

Chapter 1

Introduction

The emergence of renewable energy has drawn scientists' attention to find out more potential materials that meet the affordability and stability requirements. In this work, utilizing the rapid laser irradiation method for the fabrication and post-synthesis treatment of high entropy alloys on carbon fiber paper opens a fast, reliable method for catalysis improvements in the energy conversion field. In this chapter, the background, motivation, and problem statements are discussed to justify the potential of high entropy materials on energy conversion and storage.

1.1 Problem Statement

Energy conversion from renewable sources has been developed with recent technology through electrochemistry such as fuel cells, metal-air batteries, or water splitting. Oxygen evolution reaction (OER) is the main half-reaction involved in the reversible process along with hydrogen evolution reaction (HER) or oxygen reaction reduction (ORR) providing the other half.[1-5] To convert renewable energy sources into usable forms of energy, catalysts are essential to improve efficiency and speed up chemical reactions without being consumed in the process. In the past decades, noble metals and alloys have shown promising results on catalysts due to high catalytic activity. However, even conventional noble metal catalysts require a substantial overpotential to reach the demanded current density.[6] Furthermore, the cost to produce noble metal catalysts in the industrial and commercial market is incredibly high, which brings challenges to commercializing the research to practical energy applications. Therefore, research on cost-effective, efficient, and highly stable electrocatalysts in long-term and practical conditions is crucial and indispensable.

Recently, a novel class of high-entropy materials has raised attention to their wide variety of applications in aerospace engineering, thermoelectricity, and thermal protection, and especially electrocatalytic and electrochemical energy storage.[7-9] The lattice distortions are supportive for hydrogen storage due to increasing reaction sites for gas absorption.[8, 10-12] The presence of multi-elements lead to strong synergetic effects are beneficial to the catalysis of energy conversion process like oxygen evolution and reduction.[13, 14] The HEA charming properties give rising interests for further research and development in the field of water splitting, CO_2 reduction, supercapacitors, batteries and fuel cells.

This thesis tests and validates the design of simple hydrothermal and rapid laser irradiation process to synthesize multiple growths of high-entropy alloy nanostructures on the carbon fiber paper (CFP) substrate as highly active electrocatalysts performing the superior performance on energy conversion throughout oxygen evolution reaction.

1.2 Objectives and Scope

The use of tradition catalyst materials, such as platinum and other precious metal, can be expensive and limited in certain processes. The need for novel catalyst materials that cost-effective and have improved performance is essential. High entropy alloys have been reported for energy related applications, where the key factors are thermodynamic stability, uniform configuration of elements and many potential methods. New catalyst materials can be engineered to have higher surface area and unique crystal structure from abundant and low-cost transition metals, such as iron, cobalt, nickel, copper, etc. The applications of HEA for catalysis or energy storage and conversion have been investigated for less than a decade, which lead to lots of explorations and optimizations are necessary for future conventional prospects.

The present research is concerned with the synthesis and characterization of CoCuFeMnNi@CFP HEA to validate their oxygen evolution reaction performance and provide deeper understanding of HEA for energy conversion application. The objective is the synthesis of cost-effective, efficient, and long-term stable non-noble metals electrocatalyst by a designable and scalable laser irradiation process.

1.3 Dissertation Overview

The thesis addresses the utilization of rapid laser irradiation to synthesize multiple growths of high-entropy alloy nanostructures and perform surface modification to enhance the electrocatalytic performance in OER, which is expected to improve efficiency, lower costs, and increase the use of renewable energy resources for mitigating the impacts of the energy crisis and providing long-term benefits for the environment.

Chapter 1 provides a rationale for the research and outlines the goals and scope.

Chapter 2 reviews the literature concerning the current situation of energy crisis and highlight the beneficial of renewable energy conversion through water electrolysis. The

catalytic mechanism of OER half-reaction is reviewed. The important of materials engineering and recent research to enhance electrocatalytic are also included in this chapter. The novel high-entropy alloys, new opportunities, and strategies to improve the electrocatalytic performance of multiple metal alloys and hybrids are also reviewed.

Chapter 3 discusses the principles underlying the sample preparation, fabrication strategy, characterization and electrochemical testing techniques employed.

Chapter 4 elaborates the first major set of results. The fabrication of high-entropy alloy nanoparticles CoCuFeMnNi@CFP, including physical and electrochemical characterization. The CoCuFeMnNi@CFP HEA NPs surface morphology, element composition, crystal phase, and lattice structure will be revealed and analyzed. In addition, electrochemical tests including Linear Sweep Voltammetry, Electrochemical Impedance Spectroscopy relationship between physical and electrochemical properties will also be discussed.

Chapter 5 elaborates on the second major set of results. The high-entropy alloy nanoparticles CoCuFeMnNi@CFP have shown the promising ability in electrocatalysis for energy conversion. Nevertheless, the electrochemical activities can be enhanced further with appropriate treatment and modification. This chapter demonstrates the changes in surface morphology and composition, which result in the improvement of high-entropy alloy CoCuFeMnNi@CFP nanostructures for oxygen evolution reaction after surface modification by laser treatment. The HEAs characterization will be investigated in comparison of energy conversion effectiveness.

Chapter 6 concludes and discusses the threads of the thesis. Reconnaissance study on the effect of laser parameters on lattice structure manipulating that did not warrant a complete chapter is included. The opportunities and strategies for future work are proposed based on the current research in this thesis.

1.4 Findings and Outcomes/Originality

This research led to several novel outcomes by:

1. Demonstrating an adaptable, reliable, and effective laser irradiation to both synthesis and post-synthesis treatment of multiple growth CoCuFeMnNi@CFP high-entropy alloy nanostructures.

2. Correlating the precursor concentration with the HEA nanoparticles diameter synthesized by laser irradiation.

3. Correlating the key parameters of laser irradiation (such as mode of irradiation, power, speed, duration) to the OER performance of HEA electrocatalysts.

4. Reveal the superior OER performance of multiple growth CoCuFeMnNi@CFP HEAs after post-synthesis treatment compared to other multiple elements alloys.

References

1. Pi, Y.; Zhang, N.; Guo, S.; Guo, J.; Huang, X., Ultrathin Laminar Ir Superstructure as Highly Efficient Oxygen Evolution Electrocatalyst in Broad pH Range. *Nano Letters* **2016,** *16* (7), 4424-4430.
2. Wang, Z.-L.; Xu, D.; Xu, J.-J.; Zhang, X.-B., Oxygen electrocatalysts in metal–air batteries: from aqueous to non-aqueous electrolytes. *Chemical Society Reviews* **2014,** *43* (22), 7746-7786.
3. Huang, Z.-F.; Song, J.; Li, K.; Tahir, M.; Wang, Y.-T.; Pan, L.; Wang, L.; Zhang, X.; Zou, J.-J., Hollow Cobalt-Based Bimetallic Sulfide Polyhedra for Efficient All-pH-Value Electrochemical and Photocatalytic Hydrogen Evolution. *Journal of the American Chemical Society* **2016,** *138* (4), 1359-1365.
4. Ma, R.; Ren, X.; Xia, B. Y.; Zhou, Y.; Sun, C.; Liu, Q.; Liu, J.; Wang, J., Novel synthesis of N-doped graphene as an efficient electrocatalyst towards oxygen reduction. *Nano Research* **2016,** *9* (3), 808-819.
5. Lv, Z.; Mahmood, N.; Tahir, M.; Pan, L.; Zhang, X.; Zou, J.-J., Fabrication of zero to three dimensional nanostructured molybdenum sulfides and their electrochemical and photocatalytic applications. *Nanoscale* **2016,** *8* (43), 18250-18269.
6. Lee, Y.; Suntivich, J.; May, K. J.; Perry, E. E.; Shao-Horn, Y., Synthesis and Activities of Rutile IrO2 and RuO2 Nanoparticles for Oxygen Evolution in Acid and Alkaline Solutions. *The Journal of Physical Chemistry Letters* **2012,** *3* (3), 399-404.
7. Gao, M. C.; Miracle, D. B.; Maurice, D.; Yan, X.; Zhang, Y.; Hawk, J. A., High-entropy functional materials. *Journal of Materials Research* **2018,** *33* (19), 3138-3155.
8. Ye, Y. F.; Wang, Q.; Lu, J.; Liu, C. T.; Yang, Y., High-entropy alloy: challenges and prospects. *Materials Today* **2016,** *19* (6), 349-362.
9. Miracle, D. B.; Senkov, O. N., A critical review of high entropy alloys and related concepts. *Acta Materialia* **2017,** *122*, 448-511.
10. Kozak, R.; Sologubenko, A.; Steurer, W., Single-phase high-entropy alloys – an overview. *Zeitschrift für Kristallographie - Crystalline Materials* **2015,** *230* (1), 55-68.

11. George, E. P.; Raabe, D.; Ritchie, R. O., High-entropy alloys. *Nature Reviews Materials* **2019,** *4* (8), 515-534.
12. Gao, M.; Qiao, J., High-Entropy Alloys (HEAs). *Metals* **2018,** *8* (2).
13. Zhao, X.; Xue, Z.; Chen, W.; Wang, Y.; Mu, T., Eutectic Synthesis of High-Entropy Metal Phosphides for Electrocatalytic Water Splitting. *ChemSusChem* **2020,** *13* (8), 2038-2042.
14. Glasscott, M. W.; Pendergast, A. D.; Goines, S.; Bishop, A. R.; Hoang, A. T.; Renault, C.; Dick, J. E., Electrosynthesis of high-entropy metallic glass nanoparticles for designer, multi-functional electrocatalysis. *Nat Commun* **2019,** *10* (1), 2650.

Chapter 2

Literature Review

In this chapter, basic overviews of oxygen evolution reaction electrocatalysis in the subject of renewable energy will be discussed. The OER mechanism and influenced factors will be reviewed. State-of-the-art and novel materials for electrocatalysts and the justification of HEAs and its preference for OER will be demonstrated. At the end of this chapter, the reported performance of selected materials for OER will also be summarized.

2.1. Electrochemical Catalytic in Energy Conversion and Storage

Energy consumption and environmental sustainability grow more important concerns in the current technology and informatic era. The global demand for energy is increasing and is predicted to be doubled within the next couple of decades.[1] However, the non-renewable and unsustainable energy that comes from fossil fuels not only generates a huge amount of pollution but also causes serious economic and environmental problems. Therefore, the necessity to utilize and converse energy from green and renewable energy resources has been targeted as an earnest solution in the 21st century to expressively lessen the reliance on traditional fuels. Among several electrochemical reactions that are integrated into energy conversion technologies, fuel cells and water splitting are the most uncomplicated, reliable, and efficient in generating clean hydrogen fuels for the great renewable energy resources demand.[2]

2.1.1. Oxygen Evolution Reaction

Water oxidization or oxygen evolution reaction (OER) is the main half-reaction involved in the reversible process along with oxygen reduction reaction (ORR) and hydrogen evolution reaction (HER).[2-4] In OER, oxygen molecular is delivered through several proton-electron-coupled processes.[5-7] The pH value of the electrolyte highly affects the reaction. In neutral and acidic electrolytes, the oxidization of two water molecules (H_2O), by losing four electrons, gives four protons (H^+) and one oxygen molecule (O_2).[8] While in alkaline conditions, the hydroxyl groups (OH^-) are transformed into H_2O and O_2 with the involving of the same number of electrons.[9]

$$2\,H_2O_{(l)} \leftrightarrow 4\,H^+ + O_{2(g)} + 4e^- \qquad E_a = 1.230\,V \text{ in acidic solution}$$

$$4\,OH^- \leftrightarrow 2\,H_2O_{(l)} + O_{2(g)} + 4e^- \qquad E_a = 0.404\,V \text{ in alkaline solution}$$

OER is an electron-coupled uphill reaction, in order to create the potential difference of 1.23 V to drive the reaction at pH = 0, external energy input is required. According to Nernst equation, there is a shift of approximately 59 mV per unit pH.[5] The reversible

hydrogen electrode (RHE) is generally used as a reference electrode to avoid the pH influence and keep the working potential around 1.23 V. The oxygen molecule, which is produced from the above equation, requires the transfer of four electrons. As multiple electrons transfer is not favorable, OER goes along with one electron transfer per step via multiple steps. An accumulation of the energy barrier in each step leads to the sluggish kinetics of OER with high overpotential to overcome. Therefore, OER electrocatalysis is desired to not only have high stability and low overpotential to advance the reaction but also available for industrial scalability.[2, 10, 11]

Noble metal-based materials are one of the most valuable for their stability despite the OER rational activity. Nevertheless, in practical applications, the scarcity and costly production are major issues. Currently, extensive research efforts have been made in developing a large number of alternative materials for OER catalysts, including carbon-based materials (carbon nanotubes, carbon nanofibers, graphene, and graphene oxides), oxides, hydroxides, and alloys of earth-abundant metals (Fe, Cu, Co, Ni, Mn, etc.) and their hybrids and composites with carbon.[12-17]

2.1.2. Key Parameters Evaluating OER Performance.

Electrode

The performance of the working electrodes or substrates has a crucial impact on the reaction rate because of their varied structure, wettability, conductivity, and accessibility to an electrolyte. Depend on the electrode structure, electrode substrates are divided into two types: two-dimensional or flat electrodes and three-dimensional electrodes.

The 2D electrodes, such as Cu/Ti foil, glassy carbon (GC), and indium-doped tin oxide, permit electrolyte to interact only on the surface of catalysts. GC electrode is commonly used but provides a limited loading of catalyst and even needs a binder to stabilize the catalyst. Due to the non-conductive binders, the active sites are blocked, ion diffusion is prevented, and these results in increased the resistance, inferior wettability, and undesirable powder agglomeration.[18]

The 3D electrodes, like Ni foam, carbon cloth, and carbon paper, open multiple pathways of interaction with the electrolyte from all sides of the catalysts, which make strong electrical connection. However, directly fabricate catalyst on supportive substrate could damage or peal the catalyst due to mismatched or surface disorientation growth.[2]

Electrolyte

The OER electrocatalysis performance is extremely affected by different alkaline or acid electrolytes. Recently, many research concentrated on developing the OER electrochemical catalysts that stable in both acidic and alkaline solutions, such as transition metals oxides or hydroxides, carbon-based materials, hybrids, and intricate ternary structures.[11] However, the high oxidative potential in <7 pH solution is the obstacle for materials stability.[19]

Overpotential

Assessing the performance of OER catalysts relies primarily on their onset potential or overpotential. The value of potential at 10 $mAcm^{-2}$ is commonly used through most research and considered reliable, instead of observing the exact value due to its difficulty and complexity. Since the OER catalysts work along with RHE, overpotential, measured in mV, is the voltage/potential difference between specific current density (commonly 10 $mAcm^{-2}$) and 1.23 V. **Figure 2.1** evaluates the overpotential at the current density of 10 $mAcm^{-2}$ at t = 0 and at t = 12 h. Any material placed behind 500 mV is not good enough for OER application. A material that falls outside of the 500-mV range after 12 hours is not suitable for practical application due to its instability. Any materials lied from 300 to 400 mV especially if it still stays in this range after 12 hours are very good for OER. An ideal OER catalyst theoretically lies below 300 mV.

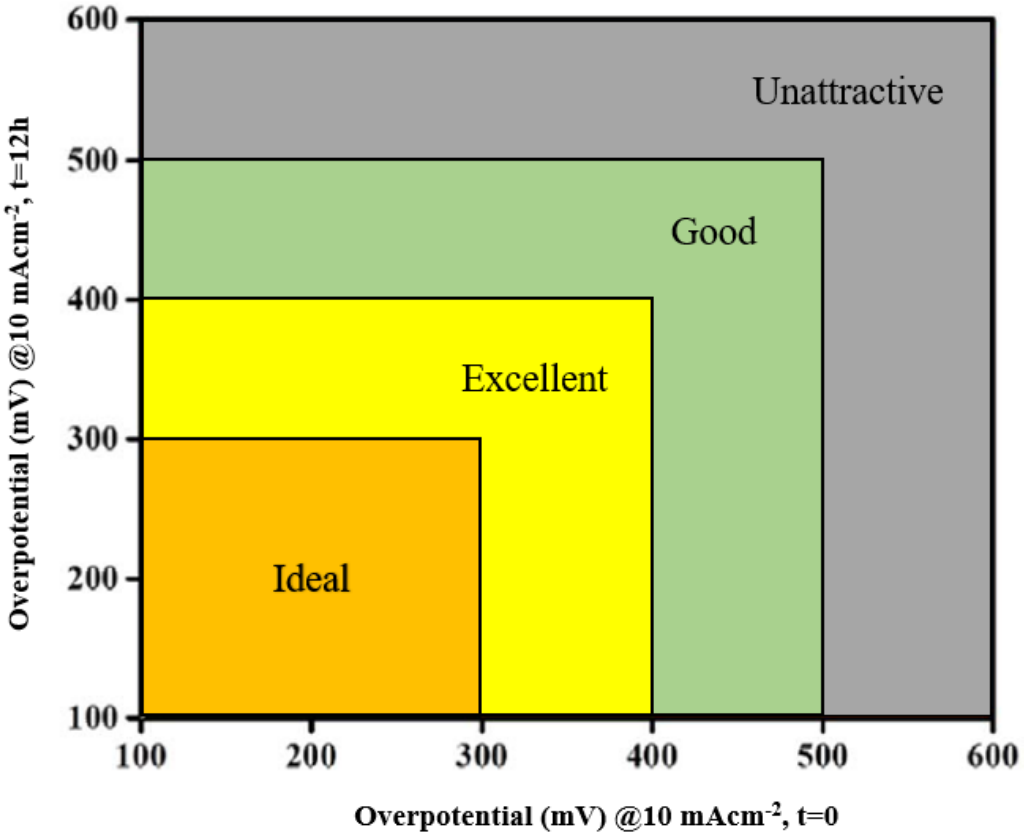

Figure 2.1: Satisfactory range for OER on overpotential performance and stability.

Tafel slope

Mechanism and reaction kinetics are analyzed by using Tafel analysis and fitting a Tafel slope. The Tafel slope is a vivid tool for comparing the catalytic efficiency between different catalysts by examining the current sensitivity.

$$\eta = \tau \times log \frac{j}{j_0}$$

Where η is the overpotential, τ represents the Tafel slope, j is the current density. A good OER performance generally presents a large current density with a low Tafel slope value.

Stability

The stability of the electrocatalyst is a crucial factor for practical applications. The nature of the working electrode and electrolyte strictly affects the catalyst stability. Most of the catalysts are stable in alkaline electrolytes but erratic in acid ones. There are several

methods to judge the stability of a catalyst to assure of applicable devices for long-term working such as brittle and hardness mechanical tests, corrosion, extreme condition test, and regular chronoamperometry or chronopotentiometry tests. Though it is hard to know the catalytic mechanism that happened during the stability test, a set of techniques including SEM, TEM, XPS, and XRD should be worked out along with potentiometric studies.

2.1.3. The Importance of OER in Energy-Related Applications.

Water splitting

Hydrogen produces only water when being combusted, which makes it a promising renewable energy resource.[19-21] Affordably and efficiently water splitting research has drawn vast attention from the last decade.[22, 23] In general, water oxidization is based on two half-reactions:

$2\,H_2O_{(l)} \rightarrow O_2 + 4\,H^+ + 4e^-$ $\qquad E = (1.230 - \ 0.059 \times pH)\ V\ vs.RHE$

$4\,H^+ + 4e^- \rightarrow 2H_2$ $\qquad E = (0 - \ 0.059 \times pH)\ V\ vs.RHE$

Overall, the process is made by a very simple equation:

$2H_2O \rightarrow 2H_2 + O_2$ $\qquad \Delta E = -1.23\ V$

The major challenge for water splitting is the bare activity of water oxidation at low potential. The research of water splitting mainly focus on developing replacement catalysts from costly and scarcity materials and improving their performance.[24]

Metal-air-battery

Metal-air batteries have high theoretical energy density and large-scale grid storage. The reversibility of metal-air battery depends on the process of oxygen evolution during OER, which can improve their energy efficiency and durability.[25, 26] Despite their great potential, the practical energy density achieved is around 21%, which only provide as 10% of traditional lithium-ion battery.[27] There are obstacles, from poor cyclic life to round-trip energy efficiency ratio between discharging and receiving.[28]

Fuel cell

A Fuel cell is an electrochemical device that generates electrical energy from the chemical energy of a fuel and an oxidizing agent, using a pair of redox reactions. Several types of fuel cells have been introduced, including solid oxides for energy storage and reversible fuel cells for the fuel resurge ability.[29-33] For instance, H_2 and O_2 and be produced from wastewater by a reversible fuel cell during the first cycle through electrocatalysis.[33] Nevertheless, the poor efficiency and stability of fuel cell despite their costly catalyst are the major obstacles to commercialize fuel cells.[34] OER is one of the standard electrochemical reactions to store the produced energy by fuel cell, which should be paid attention to develop suitable catalysts.

2.2. Materials for Electrocatalysts

Noble metals, their alloys, oxides, composites, and hybrids are the most researched catalysts for OER. Ruthenium (Ru) and iridium (Ir) experimentally showed moderately low overpotential, slight Tafel slope, and improved durability compared to palladium (Pd) and platinum (Pt).[3, 35, 36] The 3D superstructure was designed, which covers ultrathin Ir nanosheets, to improve activity and stability of Ir nanoparticles in both acidic and basic mediums.[3] For oxides, ruthenium, and iridium oxide (RuO_2, IrO_2) catalysts are widely investigated. Both are quite active for electrochemical reaction, while RuO_2 nanoparticles have higher mass activities in OER than IrO_2, showing up to 10 A/g at a potential of 1.48 V vs. RHE.[37] Ir-Ru based oxides have been fabricated by co-precipitation process in ethanol to further enhance the stability.[38]

The OER activities of earth-abundant transition metals are very much dependent on the composition, morphology, oxidation $M^{+2/+3/+4}$ states, the surface oxygen binding energy, the 3d electron number and the oxide transition enthalpy from lower to higher energy level.[25, 39, 40] For electrocatalysis, including HER, OER, and ORR, the earth-abundant transition metals are superb candidates because of the cost-effective and resourceful. Cobalt-based materials got much attention in OER applications. The activity of Co_3O_4 is highly dependent upon the morphology and oxidization state as shown by Wang et al.[15] Mesoporous Co_3O_4 NWs with oxygen vacancy on the surface lead to a higher surface area

ratio, which give more active sites that enhance the electrical conductivity as shown in **Figure 2.2**. Another candidate is nickel oxide (NiO), which is similar to cobalt oxide, devoted to improving OER performance by controlling the surface area, particle size, and microstructures.[41] Fominykh et al. synthesized ultrasmall crystalline NiO nanoparticles, created a higher oxidation state of Ni, Ni^{3+}.[42] Mixed metal oxide is another important electrocatalyst for OER. For example, Chen et al. showed excellent activity of spinel oxide with core $NiCo_2O_4$ nanowire and $NiCo_2O_4$ nanoflake as a shell on flexible conducting carbon cloth.[43] Mixed Fe-Ni electrocatalysts are observed of enhancing stability in higher oxidization state if Fe is created at the corner, edge, around Ni center.[44-46] Besides, metal hydroxides open structures allow fast diffusion with rapid electron transfer, which access catalytic active sites and enhancing electrocatalytic activity.[47] Co-Ni based hydroxides have good OER performance with high current density, low overpotential, and small Tafel slope which result of 1D morphology for electrochemically reactive surface beside octahedral coordination states.[24]

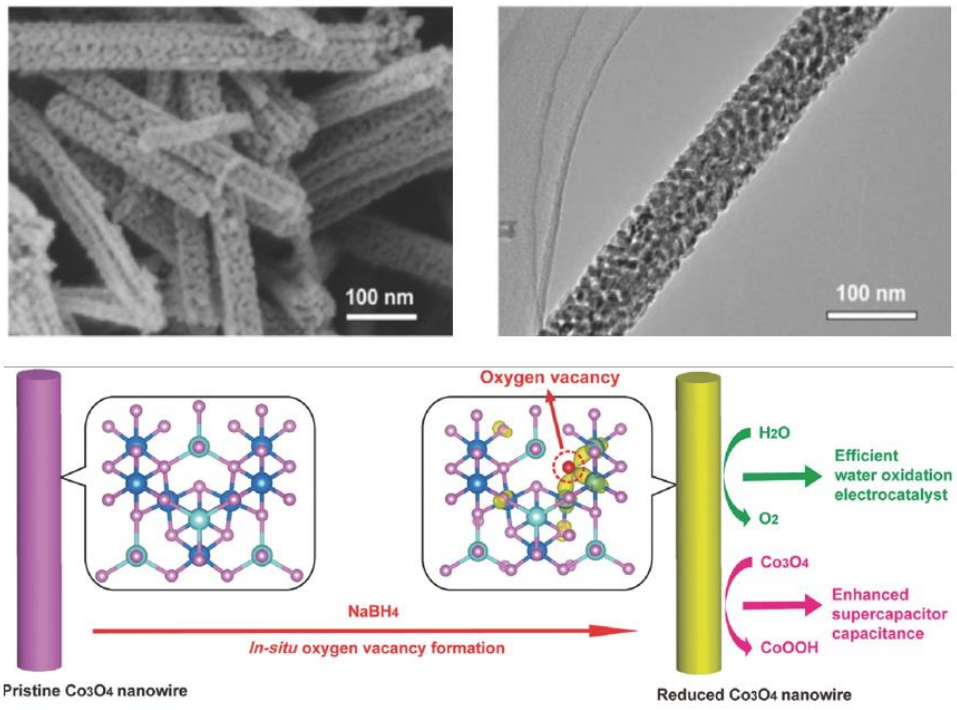

Figure 2.2. SEM and TEM of reduced Co_3O_4 NWs and schematic for in situ creation of oxygen vacancies in Co_3O_4 NWs. Copyright 2014, Advanced Energy Materials, Wang Y, no permission needed for thesis purpose.

Perovskite oxides and hydroxides with the formation of rare-earth metals or alkaline with transition metals to form a regular formula of ABO_x have also drawn major interests in OER due to the tunability and flexibility in their composition and structures.[12] Perovskite hydroxide $CoSn(OH)_6$ nano-cubes in Song's work is ideally active for OER with onset potential at a current density of 10 $mAcm^{-2}$ reached 274 mV.[48] The dissolution of Sn hydroxides has formed CoOOH hierarchical nanoporous that enhance the OER performance. Zhu et al. synthesized P-doped perovskite oxide, $SrCo_{0.95}P_{0.05}O_{3\delta}$ showed good electrical conductivity and OER activity, suggesting that crystal vacancies are important for constructing active catalysts.[12]

Hybrid nanostructures were investigated widely regarding their long-term durability, high carrier mobility, and excellent OER performance.[49] Normally, hybrids contain catalyst parts and conductive parts. The strong interface between the catalyst and the substrate in carbon-based material hybrids is the reason for the good performance. Co_3O_4 nanosheets on carbon paper (Co_3O_4@CP) are deposited through electro-planting followed by a two-step calcination process by Yang et. al. CoO and Co_3O_4 are converted from Co-species without damaging the mechanical strength between Co_3O_4 and CP interface. The extra stability of OER comes from a layer of amorphous carbon on the top surface of Co_3O_4. The mentioned catalyst has an OER overpotential of 370 mV at 10 $mAcm^{-2}$ in 0.5 M H_2SO_4.[50] The hybrids form with carbon materials not only metal oxides but also employed layered double hydroxides. Gong et al. fabricated nickel iron double-layered hydroxide on multi-walled carbon nanotubes, which is much more active in alkaline electrolytes and provided lower overpotential than commercial iridium catalysts.[10]

Graphene is another excellent monolayer carbon material that provides a large surface area and high conductivity. The graphene-based hybrids with other transition metal oxides are the excellent candidates for OER which enhance the conductivity and minimize the agglomeration.[51, 52] Mao et al. demonstrated a graphene cobalt oxide nanocrystal hybrids that have strong synergetic chemical effect for both OER and ORR.[53] The summary of recently reported electrocatalysts for OER performance is displayed in **Table 2.1**.

Table 2.1: OER performance of typical reported electrocatalysts

Catalyst	Electrode	Electrolyte	Overpotential	Tafel slope	Reference
Co_3O_4	Ni foam	1 M KOH	339	82	[54]
Co_3O_4 NWs	GC	1 M KOH	290	72	[15]
Co_3O_4@CP	CP	0.1 M KOH	310	69	[50]
Co_3O_4 NWs@CC	CC	1 M KOH	320	72	[55]
$CoNi(OH)_x$	Cu foils	1 M KOH	280	77	[24]
$CoSn(OH)_6$	GC	1 M KOH	274	-	[48]
IrO_2	GC	1 M KOH	338	47	[37]
IrO2/C	GC	0.1 M KOH	370	-	[56]
$LiCoO_2$	GC	1 M KOH	430	48	[57]
Mn Oxide	GC	0.1 M KOH	540	-	[11]
NiCo bulk	GC	1 M KOH	385	65	[58]
NiCo nanosheets	GC	1 M KOH	332	41	[58]
NiCo oxide	FTO	1 M NaOH	340	51	[59]
$NiCo_2O_4$	CC	1 M NaOH	320	47.4	[43]
N-CG-CoO	GC	1 M KOH	340	71	[53]
$ZnCo_2O_4$	CNT	0.1 M KOH	350	70.6	[60]

2.3. High-entropy Materials

Over the past decade, a new class of materials called high-entropy materials (HEMs) have been reported, which includes high-entropy oxides (HEOs), nitrides, carbides, as well as other high-entropy alloys (HEAs) and compounds. The novel group of materials has gained considerable interest and attention in the research community.[61-67] They are multicomponent of five or more near-equiatomic elements to maximize the configurational entropy and stabilize their unique coexistence structures of crystal periodicity and antisite disordering.[68] Originally, HEMs were investigated as mechanical structural materials, particularly in the aerospace, molding and tooling industries with proven abilities such as enhanced strength, extreme hardness, fracture resistance, and high elongation.[69] Moreover, the increasing global demand for energy has driven promising strategies of HEMs for electrocatalytic energy conversion applications. As previously reviewed, it is imperative to develop efficient, cost-effective, and earth-abundant nonprecious metal-based electrocatalysts as an alternative to the noble metal-based ones.[70-72] The bimetallic, trimetallic alloys, and other combinations have been given positive results in catalytic activities.[73-75] However, the development of the conventional alloys remains challenging due to the inadequate corrosion resistance in alkaline and acidic electrolyte of most transition metals.[76, 77] The contribution of multiple-element components result in larger configuration entropy to establish a single-phase solid solution structure, including body-centered cubic, face-centered cubic, hexagonal close-packing, and orthorhombic crystal structures as shown in **Figure 2.3**.[78] The atomic composition arranged with large number on the catalytic surface of HEA can boost the electrocatalytic activities by providing various surface sites linked to conversion, adsorption, and activation of reactants.[79] To this day, the research around electrocatalyst based on HEM is still at the foundation, thus opening a wide category to explore the advances of novel HEA-based electrocatalysts.

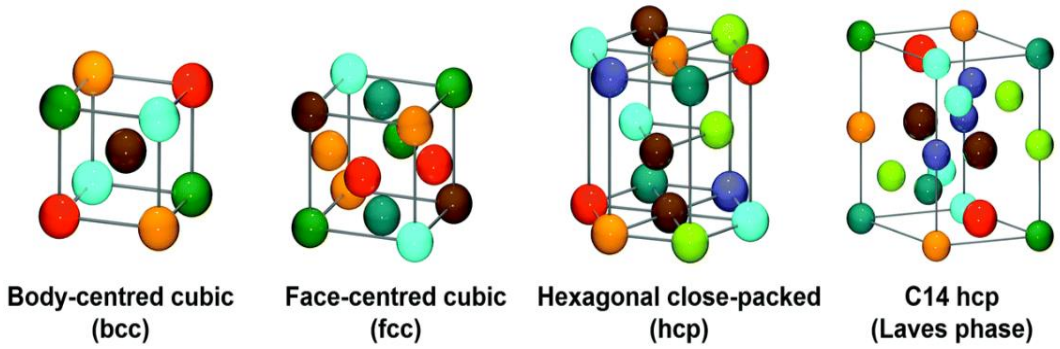

Figure 2.3. Model of high-entropy alloys crystal structures. Copyright 2021, Energy Environ. Sci., no permission needed for thesis purpose.

2.3.1. Definition and Properties of High-entropy Alloys

Generally, there are two expressions based on composition and entropy to describe high-entropy alloys. For the composition expression, HEAs indicate any alloys that contain five or more elements which atomic concentration is from 5 to 35 percent.[81] For the entropy definition, HEAs represent the mixed configuration entropy (ΔS_{mix}) as follows:[82]

$$\Delta S_{mix} = -R \sum_{i=1}^{n} x_i \ln x_i$$

where R represents the gas constant, x indicates the molar concentration of the number i elemental component. The ΔS_{mix} of HEA will reach its maximum when satisfying the equal molar ratios and can be simplified as:

$$\Delta S_{mix} = R \ln n$$

where n represents the number of elemental components in HEA. The $\Delta S_{mix} \geq 1.61R$ indicates a high-entropy alloy when $n \geq 5$. With $n = 4$ as $\Delta S_{mix} = 1.39R$ refers to quaternary alloys.[78, 81]

The characteristics and properties of HEAs have been studied by extensive efforts from recent research, which can be summarized in four core factors:

High entropy effect

The mixed configuration entropy increases correspondingly with the number of near-equimolar elemental components. The rising trend of ΔS_{mix} coming to saturation with over 9 elements alloy, at which adding more components will increase the material complexity without contributing to system entropy.[83] This effect lowers the corresponding free energy to enhance the common solubility of the elements, which facilitates the formation of a single-phase solid solution structure.[84] The rise of mixed configuration entropy can prevent the miscibility gap presented in bimetallic alloys,[85] which is beneficial to electrocatalytic properties through the uniform dispersion and elemental concentrations in the homogenous chemical environment.[86]

Sluggish diffusion effect

The difference in diffusion rates and potential energies of various elemental atoms can decrease the phase transformation and the kinetics of the diffusion in comparison to the conventional binary alloys.[87] By intervening in the surface atomic diffusion, HEAs can maintain and control the nanocrystalline structure during the synthetic process and subsequently affects the electrocatalytic performance.

Lattice distortion effect

High-entropy alloys are constructed by diverse elements with sizes difference which lead to the lattice distortion effect.[88] The small atoms can be distributed to additional space while the large atoms will occupy more space and push neighbour atoms away, which results in lattice strain and compression. In some cases, the stronger bonds prevent dislocation slipping and consequently enhance the mechanical properties,[89] while in other cases, weaker bonds lead to the collapse of lattice and form amorphous structure.[90] Although thermal and electrical conductivity can be lowered due to increasing phonon scattering from lattice distortion, the mismatch of atomic sizes could decrease the energy gap for adsorption and activation in electrocatalytic process.[91]

Synergy effect

This is a complicated characteristic influenced by the three above properties which are affected by not only the properties of individual elements but also the interaction between components that could not be manifested by any independent element. For example, when most of the components are light, the overall density of HEAs decreases while improving the antioxidant activity after presenting a strong antioxidative metallic element.[92] Another example for $CoCrFeNiAl_x$ HEAs form stronger bonds between Al and other elements, which significantly harden the alloy despite the low melting point of Al.[93] The synergy effect has great potential to enhance electrocatalytic activity by achieving the synergy and tunability of mixed highly active transition metal components.[94]

2.3.2. Electrocatalytic Oxygen Evolution Reaction of HEAs

Recent investigations of HEAs demonstrated promising OER electrocatalysts. Qiu et al. synthesized a nanoporous Ir-based quinary AlNiCoIrX (X = Cr, Cu, Mo, Nb, V) HEAs using alloying and dealloying process.[95] The synergy effect from these elemental components leads to remarkable OER overpotential of 233 mV at 10 $mAcm^{-2}$ and a small Tafel slope of 55.2 $mVdec^{-1}$ using AlNiCoIrMo HEA. The superb performance is the result of the Ir-O bond covalency increasing by the synergy effect from nickel and X with other elements. Ting et al. synthesized high-entropy perovskite oxide (HEPO) containing five consecutive first-row transition metals (Cr, Mn, Fe, Co, and Ni) by using a facile coprecipitation method. The result showed an OER overpotential of 325 mV at 10 $mAcm^{-2}$, Tafel slope of 51.2 $mVdec^{-1}$, and excellent stability for 50 hours.[96] Mu et al. introduced a HE-MOFs with five near-equimolar components (Co, Cu, Fe, Mn, and Ni) under ambient temperature by combining features between abundant metal sites and ultrathin structure in MOF with synergy effect in HEAs, acquiring overpotential of 245 mV at 10 $mAcm^{-2}$ but have a slight decay of current (~4.9%) after 48 hours.[97] Some other works of HEAs for OER application are summarized in **Table 2.2**.

Table 2.2: OER performance of typical reported high-entropy materials

Catalysts	Synthesis	Electrolyte	Overpotential at 10mAcm^{-2}	Tafel slope	Ref.
MnFeCoNi	Mechanical alloying	1 M KOH	302	83.7	[98]
FeCoNiCuZn	Electrochemical reduction	1 M KOH	340	48	[99]
CoCrFeNiMo	Microwave sintering	1 M KOH	220	59	[100]
AlCrFeNiCu	Induction melting	1 M KOH	270	77.5	[101]
FeCoNiCrNb	Dealloying	0.1 M KOH	288	27.7	[102]
CoCuFeMnNiO	Solvothermal	1 M KOH	350	76.7	[103]
CoNiMnZnFeO	Mechanical alloying	1 M KOH	336	47.5	[104]
CoCrFeMnNiP	Eutectic	1 M KOH	320	60.8	[86]
CoFeLaNiPt	Electro-shock	0.1 M KOH	377	150	[105]

As illustrated in **Table 2.2**, various synthesis methods have been used to fabricate transition metal alloys or HEAs. Each of the strategies have their own unique advantages and limitations.

Mechanical alloying provides advantages such as homogenous mixing, a broad range of compositions and solid solubility. The downsides are longer processing time, consumes more energy, and a risk of contamination.[98,104]

Electrochemical reduction allows selective and precisely controlled of metal ions as well as the composition. The process can be performed at relatively low temperature. However, it is confined to specific materials and required specialize equipment and expertise.[99]

Microwave sintering offers rapid heating with short processing time as well as improved mechanical properties and densification. Materials limitations of appropriate dielectric properties can cause inconsistent heating.[100]

Induction melting allows for rapid and exact control over temperature and heating rate, but it is limited to conductive materials and has a high initial equipment cost.[101]

Solvothermal has the ability to synthesize nanomaterials with controlled size and morphology. It also has access to wide range of materials and composition and controllable over certain chemical reactions. The challenges lie in removing solvent residues, especially organics solvent which requires safety precautions.[103]

Thermal shock provides rapid heating and quenching, which can efficiently decompose the salts mixture to induces structural and phase transformation.[1]

Researchers can make informed decisions that fit with their desired outcomes by examining the advantages and disadvantages of each synthesis process, whether it is improving material qualities, obtaining precise compositions, or assuring efficient and scalable production to meet the specific needs of their applications.

2.3.3. Surface Modification for Electrocatalysts

Even though several sophisticated new materials have been reported to demonstrate exceptional electrocatalytic performance in water electrolysis, the majority of them are still far from practical applications due to their limited catalytic activities. Catalysis is commonly regarded as a surface reaction. There are two strategies for increasing electrocatalytic activity: (1) increasing the number of active sites on the electrocatalyst

surface, such as nanosized structures with high surface ratio; and (2) increasing the intrinsic activity of each active site on the electrocatalyst surface, such as doping and vacancy engineering.[2,3] Many efforts have been undertaken to improve electrocatalyst performance by surface modification. Defect engineering and alloying engineering are extensively utilized methodologies to improve the catalytic activity of active sites in transition metal alloy/oxide materials.

Defects in crystal structures and lattice such as lattice strain[109-111], dislocations[112-113], and vacancies[107,114] have been reported to provide supplementary ability to modify the properties of a crystal. Vacancies have received a lot of attention in defect engineering of electrocatalysts because of the electronic structure, characteristics, and performance may be modified by altering their concentration, distribution, and charge.[107] Vacancy is also the most frequently found defect in observation because most synthesis processes use high temperatures, which promotes the development of vacancy defects. As a result, post-thermal treatment has become a popular way for manipulating defects for electrocatalysts.

References

1. Chow, J.; Kopp, R. J.; Portney, P. R., Energy Resources and Global Development. *Science* **2003,** *302* (5650), 1528-1531.
2. Tahir, M.; Pan, L.; Idrees, F.; Zhang, X.; Wang, L.; Zou, J.-J.; Wang, Z. L., Electrocatalytic oxygen evolution reaction for energy conversion and storage: A comprehensive review. *Nano Energy* **2017,** *37*, 136-157.
3. Pi, Y.; Zhang, N.; Guo, S.; Guo, J.; Huang, X., Ultrathin Laminar Ir Superstructure as Highly Efficient Oxygen Evolution Electrocatalyst in Broad pH Range. *Nano Letters* **2016,** *16* (7), 4424-4430.
4. Ma, R.; Ren, X.; Xia, B. Y.; Zhou, Y.; Sun, C.; Liu, Q.; Liu, J.; Wang, J., Novel synthesis of N-doped graphene as an efficient electrocatalyst towards oxygen reduction. *Nano Research* **2016,** *9* (3), 808-819.
5. Gong, M.; Dai, H., A mini review of NiFe-based materials as highly active oxygen evolution reaction electrocatalysts. *Nano Research* **2015,** *8* (1), 23-39.
6. Oh, K. Electrochemical nanostructuration of silicon for energy applications. 2020.
7. Busch, M.; Halck, N. B.; Kramm, U. I.; Siahrostami, S.; Krtil, P.; Rossmeisl, J., Beyond the top of the volcano? – A unified approach to electrocatalytic oxygen reduction and oxygen evolution. *Nano Energy* **2016,** *29*, 126-135.
8. Conway, B. E.; Liu, T. C., Characterization of electrocatalysis in the oxygen evolution reaction at platinum by evaluation of behavior of surface intermediate states at the oxide film. *Langmuir* **1990,** *6* (1), 268-276.
9. Birss, V. I.; Damjanovic, A.; Hudson, P. G., Oxygen Evolution at Platinum Electrodes in Alkaline Solutions: II . Mechanism of the Reaction. *Journal of The Electrochemical Society* **1986,** *133* (8), 1621-1625.
10. Gong, M.; Li, Y.; Wang, H.; Liang, Y.; Wu, J. Z.; Zhou, J.; Wang, J.; Regier, T.; Wei, F.; Dai, H., An Advanced Ni–Fe Layered Double Hydroxide Electrocatalyst for Water Oxidation. *Journal of the American Chemical Society* **2013,** *135* (23), 8452-8455.

11. Gorlin, Y.; Jaramillo, T. F., A Bifunctional Nonprecious Metal Catalyst for Oxygen Reduction and Water Oxidation. *Journal of the American Chemical Society* **2010,** *132* (39), 13612-13614.
12. Zhu, Y.; Zhou, W.; Sunarso, J.; Zhong, Y.; Shao, Z., Phosphorus-Doped Perovskite Oxide as Highly Efficient Water Oxidation Electrocatalyst in Alkaline Solution. *Advanced Functional Materials* **2016,** *26* (32), 5862-5872.
13. Feng, J.-X.; Ye, S.-H.; Xu, H.; Tong, Y.-X.; Li, G.-R., Design and Synthesis of FeOOH/CeO2 Heterolayered Nanotube Electrocatalysts for the Oxygen Evolution Reaction. *Advanced Materials* **2016,** *28* (23), 4698-4703.
14. Bergmann, A.; Zaharieva, I.; Dau, H.; Strasser, P., Electrochemical water splitting by layered and 3D cross-linked manganese oxides: correlating structural motifs and catalytic activity. *Energy & Environmental Science* **2013,** *6* (9), 2745-2755.
15. Wang, Y.; Zhou, T.; Jiang, K.; Da, P.; Peng, Z.; Tang, J.; Kong, B.; Cai, W.-B.; Yang, Z.; Zheng, G., Reduced Mesoporous Co3O4 Nanowires as Efficient Water Oxidation Electrocatalysts and Supercapacitor Electrodes. *Advanced Energy Materials* **2014,** *4* (16), 1400696.
16. Li, Y.; Hasin, P.; Wu, Y., NixCo3−xO4 Nanowire Arrays for Electrocatalytic Oxygen Evolution. *Advanced Materials* **2010,** *22* (17), 1926-1929.
17. Tahir, M.; Mahmood, N.; Pan, L.; Huang, Z.-F.; Lv, Z.; Zhang, J.; Butt, F. K.; Shen, G.; Zhang, X.; Dou, S. X.; Zou, J.-J., Efficient water oxidation through strongly coupled graphitic C3N4 coated cobalt hydroxide nanowires. *Journal of Materials Chemistry A* **2016,** *4* (33), 12940-12946.
18. Masa, J.; Weide, P.; Peeters, D.; Sinev, I.; Xia, W.; Sun, Z.; Somsen, C.; Muhler, M.; Schuhmann, W., Amorphous Cobalt Boride (Co2B) as a Highly Efficient Nonprecious Catalyst for Electrochemical Water Splitting: Oxygen and Hydrogen Evolution. *Advanced Energy Materials* **2016,** *6* (6), 1502313.
19. Roy Chowdhury, S.; Ray, A.; Chougule, S. S.; Min, J.; Jeffery, A. A.; Ko, K.; Kim, Y.; Das, S.; Jung, N., Mixed Spinel Ni–Co Oxides: An Efficient Bifunctional Oxygen Electrocatalyst for Sustainable Energy Application. *ACS Applied Energy Materials* **2022,** *5* (4), 4421-4430.

20. Du, P.; Eisenberg, R., Catalysts made of earth-abundant elements (Co, Ni, Fe) for water splitting: Recent progress and future challenges. *Energy & Environmental Science* **2012,** *5* (3), 6012-6021.
21. S. R. Narayan, A. K. M., and Sanjeev Mukerjee, Bi-functional Oxygen Electrodes - Challenges and Prospects. *The Electrochemical Society* **2015**.
22. Kibsgaard, J.; Jaramillo, T. F., Molybdenum Phosphosulfide: An Active, Acid-Stable, Earth-Abundant Catalyst for the Hydrogen Evolution Reaction. *Angewandte Chemie International Edition* **2014,** *53* (52), 14433-14437.
23. Jahan, M.; Liu, Z.; Loh, K. P., A Graphene Oxide and Copper-Centered Metal Organic Framework Composite as a Tri-Functional Catalyst for HER, OER, and ORR. *Advanced Functional Materials* **2013,** *23* (43), 5363-5372.
24. Li, S.; Wang, Y.; Peng, S.; Zhang, L.; Al-Enizi, A. M.; Zhang, H.; Sun, X.; Zheng, G., Co–Ni-Based Nanotubes/Nanosheets as Efficient Water Splitting Electrocatalysts. *Advanced Energy Materials* **2016,** *6* (3), 1501661.
25. Yang, Y.; Fei, H.; Ruan, G.; Xiang, C.; Tour, J. M., Efficient Electrocatalytic Oxygen Evolution on Amorphous Nickel–Cobalt Binary Oxide Nanoporous Layers. *ACS Nano* **2014,** *8* (9), 9518-9523.
26. Guo, Y.; Tong, Y.; Chen, P.; Xu, K.; Zhao, J.; Lin, Y.; Chu, W.; Peng, Z.; Wu, C.; Xie, Y., Engineering the Electronic State of a Perovskite Electrocatalyst for Synergistically Enhanced Oxygen Evolution Reaction. *Advanced Materials* **2015,** *27* (39), 5989-5994.
27. Gao, X.; Zhang, H.; Li, Q.; Yu, X.; Hong, Z.; Zhang, X.; Liang, C.; Lin, Z., Hierarchical NiCo2O4 Hollow Microcuboids as Bifunctional Electrocatalysts for Overall Water-Splitting. *Angewandte Chemie International Edition* **2016,** *55* (21), 6290-6294.
28. Farooq, M. U.; Butt, S.; Gao, K.; Sun, X.; Pang, X.; Khan, S. U.; Xu, W.; Mohmed, F.; Mahmood, A.; Mahmood, N., Enhanced thermoelectric efficiency of Cu2−xSe–Cu2S composite by incorporating Cu2S nanoparticles. *Ceramics International* **2016,** *42* (7), 8395-8401.

29. Mahmood, N.; Zhang, C.; Yin, H.; Hou, Y., Graphene-based nanocomposites for energy storage and conversion in lithium batteries, supercapacitors and fuel cells. *Journal of Materials Chemistry A* **2014,** *2* (1), 15-32.
30. Yu, E. H.; Wang, X.; Krewer, U.; Li, L.; Scott, K., Direct oxidation alkaline fuel cells: from materials to systems. *Energy & Environmental Science* **2012,** *5* (2), 5668-5680.
31. Li, Q.; Mahmood, N.; Zhu, J.; Hou, Y.; Sun, S., Graphene and its composites with nanoparticles for electrochemical energy applications. *Nano Today* **2014,** *9* (5), 668-683.
32. Shih, Z.-Y.; Periasamy, A. P.; Hsu, P.-C.; Chang, H.-T., Synthesis and catalysis of copper sulfide/carbon nanodots for oxygen reduction in direct methanol fuel cells. *Applied Catalysis B: Environmental* **2013,** *132-133*, 363-369.
33. Saadi, A.; Becherif, M.; Aboubou, A.; Ayad, M. Y., Comparison of proton exchange membrane fuel cell static models. *Renewable Energy* **2013,** *56*, 64-71.
34. Sengodan, S.; Choi, S.; Jun, A.; Shin, T. H.; Ju, Y.-W.; Jeong, H. Y.; Shin, J.; Irvine, J. T. S.; Kim, G., Layered oxygen-deficient double perovskite as an efficient and stable anode for direct hydrocarbon solid oxide fuel cells. *Nature Materials* **2015,** *14* (2), 205-209.
35. Jiao, Y.; Zheng, Y.; Jaroniec, M.; Qiao, S. Z., Design of electrocatalysts for oxygen- and hydrogen-involving energy conversion reactions. *Chemical Society Reviews* **2015,** *44* (8), 2060-2086.
36. Reier, T.; Oezaslan, M.; Strasser, P., Electrocatalytic Oxygen Evolution Reaction (OER) on Ru, Ir, and Pt Catalysts: A Comparative Study of Nanoparticles and Bulk Materials. *ACS Catalysis* **2012,** *2* (8), 1765-1772.
37. Lee, Y.; Suntivich, J.; May, K. J.; Perry, E. E.; Shao-Horn, Y., Synthesis and Activities of Rutile IrO2 and RuO2 Nanoparticles for Oxygen Evolution in Acid and Alkaline Solutions. *The Journal of Physical Chemistry Letters* **2012,** *3* (3), 399-404.
38. Audichon, T.; Mayousse, E.; Morisset, S.; Morais, C.; Comminges, C.; Napporn, T. W.; Kokoh, K. B., Electroactivity of RuO2–IrO2 mixed nanocatalysts toward the oxygen evolution reaction in a water electrolyzer supplied by a solar profile. *International Journal of Hydrogen Energy* **2014,** *39* (30), 16785-16796.

39. Yang, J.; Cooper, J. K.; Toma, F. M.; Walczak, Karl A.; Favaro, M.; Beeman, Jeffrey W.; Hess, Lucas H.; Wang, C.; Zhu, C.; Gul, S.; Yano, J.; Kisielowski, C.; Schwartzberg, A.; Sharp, Ian D., A multifunctional biphasic water splitting catalyst tailored for integration with high-performance semiconductor photoanodes. *Nature Materials* **2017,** *16* (3), 335-341.
40. Zhang, M.; de Respinis, M.; Frei, H., Time-resolved observations of water oxidation intermediates on a cobalt oxide nanoparticle catalyst. *Nature Chemistry* **2014,** *6* (4), 362-367.
41. Han, L.; Dong, S.; Wang, E., Transition-Metal (Co, Ni, and Fe)-Based Electrocatalysts for the Water Oxidation Reaction. *Advanced Materials* **2016,** *28* (42), 9266-9291.
42. Fominykh, K.; Feckl, J. M.; Sicklinger, J.; Döblinger, M.; Böcklein, S.; Ziegler, J.; Peter, L.; Rathousky, J.; Scheidt, E.-W.; Bein, T.; Fattakhova-Rohlfing, D., Ultrasmall Dispersible Crystalline Nickel Oxide Nanoparticles as High-Performance Catalysts for Electrochemical Water Splitting. *Advanced Functional Materials* **2014,** *24* (21), 3123-3129.
43. Chen, R.; Wang, H. Y.; Miao, J.; Yang, H.; Liu, B., A flexible high-performance oxygen evolution electrode with three-dimensional NiCo2O4 core-shell nanowires. *Nano Energy* **2015,** *11*, 333-340.
44. Smith, R. D. L.; Prévot, M. S.; Fagan, R. D.; Trudel, S.; Berlinguette, C. P., Water Oxidation Catalysis: Electrocatalytic Response to Metal Stoichiometry in Amorphous Metal Oxide Films Containing Iron, Cobalt, and Nickel. *Journal of the American Chemical Society* **2013,** *135* (31), 11580-11586.
45. Fominykh, K.; Chernev, P.; Zaharieva, I.; Sicklinger, J.; Stefanic, G.; Döblinger, M.; Müller, A.; Pokharel, A.; Böcklein, S.; Scheu, C.; Bein, T.; Fattakhova-Rohlfing, D., Iron-Doped Nickel Oxide Nanocrystals as Highly Efficient Electrocatalysts for Alkaline Water Splitting. *ACS Nano* **2015,** *9* (5), 5180-5188.
46. Görlin, M.; Chernev, P.; Ferreira de Araújo, J.; Reier, T.; Dresp, S.; Paul, B.; Krähnert, R.; Dau, H.; Strasser, P., Oxygen Evolution Reaction Dynamics, Faradaic Charge Efficiency, and the Active Metal Redox States of Ni–Fe Oxide Water

Splitting Electrocatalysts. *Journal of the American Chemical Society* **2016,** *138* (17), 5603-5614.

47. Gao, M.; Sheng, W.; Zhuang, Z.; Fang, Q.; Gu, S.; Jiang, J.; Yan, Y., Efficient Water Oxidation Using Nanostructured α-Nickel-Hydroxide as an Electrocatalyst. *Journal of the American Chemical Society* **2014,** *136* (19), 7077-7084.
48. Song, F.; Schenk, K.; Hu, X., A nanoporous oxygen evolution catalyst synthesized by selective electrochemical etching of perovskite hydroxide CoSn(OH)6 nanocubes. *Energy & Environmental Science* **2016,** *9* (2), 473-477.
49. Zhu, Y. P.; Guo, C.; Zheng, Y.; Qiao, S.-Z., Surface and Interface Engineering of Noble-Metal-Free Electrocatalysts for Efficient Energy Conversion Processes. *Accounts of Chemical Research* **2017,** *50* (4), 915-923.
50. Yang, X.; Li, H.; Lu, A.-Y.; Min, S.; Idriss, Z.; Hedhili, M. N.; Huang, K.-W.; Idriss, H.; Li, L.-J., Highly acid-durable carbon coated Co3O4 nanoarrays as efficient oxygen evolution electrocatalysts. *Nano Energy* **2016,** *25*, 42-50.
51. Tang, C.; Wang, H.-S.; Wang, H.-F.; Zhang, Q.; Tian, G.-L.; Nie, J.-Q.; Wei, F., Spatially Confined Hybridization of Nanometer-Sized NiFe Hydroxides into Nitrogen-Doped Graphene Frameworks Leading to Superior Oxygen Evolution Reactivity. *Advanced Materials* **2015,** *27* (30), 4516-4522.
52. Liang, Y.; Li, Y.; Wang, H.; Zhou, J.; Wang, J.; Regier, T.; Dai, H., Co3O4 nanocrystals on graphene as a synergistic catalyst for oxygen reduction reaction. *Nature Materials* **2011,** *10* (10), 780-786.
53. Mao, S.; Wen, Z.; Huang, T.; Hou, Y.; Chen, J., High-performance bi-functional electrocatalysts of 3D crumpled graphene–cobalt oxide nanohybrids for oxygen reduction and evolution reactions. *Energy & Environmental Science* **2014,** *7* (2), 609-616.
54. Zhang, Y.; Ouyang, B.; Xu, J.; Jia, G.; Chen, S.; Rawat, R. S.; Fan, H. J., Rapid Synthesis of Cobalt Nitride Nanowires: Highly Efficient and Low-Cost Catalysts for Oxygen Evolution. *Angewandte Chemie International Edition* **2016,** *55* (30), 8670-8674.
55. Chen, P.; Xu, K.; Fang, Z.; Tong, Y.; Wu, J.; Lu, X.; Peng, X.; Ding, H.; Wu, C.; Xie, Y., Metallic Co4N Porous Nanowire Arrays Activated by Surface Oxidation

as Electrocatalysts for the Oxygen Evolution Reaction. *Angewandte Chemie International Edition* **2015,** *54* (49), 14710-14714.

56. Zhao, Y.; Nakamura, R.; Kamiya, K.; Nakanishi, S.; Hashimoto, K., Nitrogen-doped carbon nanomaterials as non-metal electrocatalysts for water oxidation. *Nature Communications* **2013,** *4* (1), 2390.
57. Gardner, G.; Al-Sharab, J.; Danilovic, N.; Go, Y. B.; Ayers, K.; Greenblatt, M.; Charles Dismukes, G., Structural basis for differing electrocatalytic water oxidation by the cubic, layered and spinel forms of lithium cobalt oxides. *Energy & Environmental Science* **2016,** *9* (1), 184-192.
58. Song, F.; Hu, X., Exfoliation of layered double hydroxides for enhanced oxygen evolution catalysis. *Nature Communications* **2014,** *5* (1), 4477.
59. Wang, H. Y.; Hsu, Y. Y.; Chen, R.; Chan, T. S.; Chen, H. M.; Liu, B., Ni3+-Induced Formation of Active NiOOH on the Spinel Ni–Co Oxide Surface for Efficient Oxygen Evolution Reaction. *Advanced Energy Materials* **2015,** *5* (10), 1500091.
60. Liu, Z.-Q.; Cheng, H.; Li, N.; Ma, T. Y.; Su, Y. Z., ZnCo2O4 Quantum Dots Anchored on Nitrogen-Doped Carbon Nanotubes as Reversible Oxygen Reduction/Evolution Electrocatalysts. *Advanced Materials* **2016,** *28* (19), 3777-3784.
61. Jin, T.; Sang, X.; Unocic, R. R.; Kinch, R. T.; Liu, X.; Hu, J.; Liu, H.; Dai, S., Mechanochemical-Assisted Synthesis of High entropyMetal Nitride via a Soft Urea Strategy. *Advanced Materials* **2018,** *30* (23), 1707512.
62. Yan, X.; Constantin, L.; Lu, Y.; Silvain, J.-F.; Nastasi, M.; Cui, B., (Hf0.2Zr0.2Ta0.2Nb0.2Ti0.2)C high entropyceramics with low thermal conductivity. *Journal of the American Ceramic Society* **2018,** *101* (10), 4486-4491.
63. Dąbrowa, J.; Stygar, M.; Mikuła, A.; Knapik, A.; Mroczka, K.; Tejchman, W.; Danielewski, M.; Martin, M., Synthesis and microstructure of the (Co,Cr,Fe,Mn,Ni)3O4 high entropy oxide characterized by spinel structure. *Materials Letters* **2018,** *216*, 32-36.
64. Sarkar, A.; Wang, Q.; Schiele, A.; Chellali, M. R.; Bhattacharya, S. S.; Wang, D.; Brezesinski, T.; Hahn, H.; Velasco, L.; Breitung, B., High entropyOxides:

Fundamental Aspects and Electrochemical Properties. *Advanced Materials* **2019,** *31* (26), 1806236.

65. Rost, C. M.; Sachet, E.; Borman, T.; Moballegh, A.; Dickey, E. C.; Hou, D.; Jones, J. L.; Curtarolo, S.; Maria, J.-P., Entropy-stabilized oxides. *Nature Communications* **2015,** *6* (1), 8485.
66. George, E. P.; Raabe, D.; Ritchie, R. O., High entropyalloys. *Nature Reviews Materials* **2019,** *4* (8), 515-534.
67. Gao, M. C.; Miracle, D. B.; Maurice, D.; Yan, X.; Zhang, Y.; Hawk, J. A., High entropyfunctional materials. *Journal of Materials Research* **2018,** *33* (19), 3138-3155.
68. Fu, M.; Ma, X.; Zhao, K.; Li, X.; Su, D., High entropy materials for energy-related applications. *iScience* **2021,** *24* (3), 102177.
69. Dada, M.; Popoola, P.; Mathe, N., Recent advances of high-entropy alloys for aerospace applications: a review. *World Journal of Engineering* **2021**.
70. Zhang, P.; Liu, Y.; Liang, T.; Ang, E. H.; Zhang, X.; Ma, F.; Dai, Z., Nitrogen-doped carbon wrapped Co-Mo2C dual Mott–Schottky nanosheets with large porosity for efficient water electrolysis. *Applied Catalysis B: Environmental* **2021,** *284*, 119738.
71. Wang, X.; Li, Z.; Wu, D.-Y.; Shen, G. R.; Zou, C.; Feng, Y.; Liu, H.; Dong, C.-K.; Du, X.-W., Porous Cobalt–Nickel Hydroxide Nanosheets with Active Cobalt Ions for Overall Water Splitting. *Small* **2019,** *15* (8), 1804832.
72. Feng, C.; Faheem, M. B.; Fu, J.; Xiao, Y.; Li, C.; Li, Y., Fe-Based Electrocatalysts for Oxygen Evolution Reaction: Progress and Perspectives. *ACS Catalysis* **2020,** *10* (7), 4019-4047.
73. Dinh, K. N.; Zheng, P.; Dai, Z.; Zhang, Y.; Dangol, R.; Zheng, Y.; Li, B.; Zong, Y.; Yan, Q., Ultrathin Porous NiFeV Ternary Layer Hydroxide Nanosheets as a Highly Efficient Bifunctional Electrocatalyst for Overall Water Splitting. *Small* **2018,** *14* (8), 1703257.
74. Luo, W. B.; Pham, T. V.; Guo, H. P.; Liu, H. K.; Dou, S. X., Three-Dimensional Array of TiN@Pt3Cu Nanowires as an Efficient Porous Electrode for the Lithium–Oxygen Battery. *ACS Nano* **2017,** *11* (2), 1747-1754.

75. Yang, F.; Kang, N.; Yan, J.; Wang, X.; He, J.; Huo, S.; Song, L., Hydrogen Evolution Reaction Property of Molybdenum Disulfide/Nickel Phosphide Hybrids in Alkaline Solution. *Metals* **2018,** *8*, 359.
76. Geiger, S.; Kasian, O.; Ledendecker, M.; Pizzutilo, E.; Mingers, A. M.; Fu, W. T.; Diaz-Morales, O.; Li, Z.; Oellers, T.; Fruchter, L.; Ludwig, A.; Mayrhofer, K. J. J.; Koper, M. T. M.; Cherevko, S., The stability number as a metric for electrocatalyst stability benchmarking. *Nature Catalysis* **2018,** *1* (7), 508-515.
77. Cherevko, S.; Geiger, S.; Kasian, O.; Kulyk, N.; Grote, J.-P.; Savan, A.; Shrestha, B. R.; Merzlikin, S.; Breitbach, B.; Ludwig, A.; Mayrhofer, K. J. J., Oxygen and hydrogen evolution reactions on Ru, RuO2, Ir, and IrO2 thin film electrodes in acidic and alkaline electrolytes: A comparative study on activity and stability. *Catalysis Today* **2016,** *262*, 170-180.
78. Miracle, D. B.; Senkov, O. N., A critical review of high-entropy alloys and related concepts. *Acta Materialia* **2017,** *122*, 448-511.
79. Kumar Katiyar, N.; Biswas, K.; Yeh, J.-W.; Sharma, S.; Sekhar Tiwary, C., A perspective on the catalysis using the high-entropy alloys. *Nano Energy* **2021,** *88*, 106261.
80. Ma, Y.; Ma, Y.; Wang, Q.; Schweidler, S.; Botros, M.; Fu, T.; Hahn, H.; Brezesinski, T.; Breitung, B., High entropyenergy materials: challenges and new opportunities. *Energy & Environmental Science* **2021,** *14* (5), 2883-2905.
81. Yeh, J. W.; Chen, S. K.; Lin, S. J.; Gan, J. Y.; Chin, T. S.; Shun, T. T.; Tsau, C. H.; Chang, S. Y., Nanostructured High entropyAlloys with Multiple Principal Elements: Novel Alloy Design Concepts and Outcomes. *Advanced Engineering Materials* **2004,** *6* (5), 299-303.
82. Fultz, B., Vibrational thermodynamics of materials. *Progress in Materials Science* **2010,** *55* (4), 247-352.
83. Yeh, J. W., Alloy Design Strategies and Future Trends in High entropyAlloys. *JOM* **2013,** *65* (12), 1759-1771.
84. Cantor, B.; Chang, I. T. H.; Knight, P.; Vincent, A. J. B., Microstructural development in equiatomic multicomponent alloys. *Materials Science and Engineering: A* **2004,** *375-377*, 213-218.

85. Xie, P.; Yao, Y.; Huang, Z.; Liu, Z.; Zhang, J.; Li, T.; Wang, G.; Shahbazian-Yassar, R.; Hu, L.; Wang, C., Highly efficient decomposition of ammonia using high entropyalloy catalysts. *Nature Communications* **2019,** *10* (1), 4011.
86. Zhao, X.; Xue, Z.; Chen, W.; Wang, Y.; Mu, T., Eutectic Synthesis of High entropyMetal Phosphides for Electrocatalytic Water Splitting. *ChemSusChem* **2020,** *13* (8), 2038-2042.
87. Tsai, K. Y.; Tsai, M. H.; Yeh, J. W., Sluggish diffusion in Co–Cr–Fe–Mn–Ni high entropyalloys. *Acta Materialia* **2013,** *61* (13), 4887-4897.
88. He, Q.; Yang, Y., On Lattice Distortion in High-entropy alloys. *Frontiers in Materials* **2018,** *5*.
89. Chen, Y.; Fu, H.; Huang, Y.; Huang, L.; Zheng, X.; Dai, Y.; Huang, Y.; Luo, W., Opportunities for High entropy materials in Rechargeable Batteries. *ACS Materials Letters* **2021,** *3* (2), 160-170.
90. Yao, Y.; Liu, Z.; Xie, P.; Huang, Z.; Li, T.; Morris, D.; Finfrock, Z.; Zhou, J.; Jiao, M.; Gao, J.; Mao, Y.; Miao, J.; Zhang, P.; Shahbazian-Yassar, R.; Wang, C.; Wang, G.; Hu, L., Computationally aided, entropy-driven synthesis of highly efficient and durable multi-elemental alloy catalysts. *Science Advances 6* (11), eaaz0510.
91. Lv, Z. Y.; Liu, X. J.; Jia, B.; Wang, H.; Wu, Y.; Lu, Z. P., Development of a novel high entropyalloy with eminent efficiency of degrading azo dye solutions. *Scientific Reports* **2016,** *6* (1), 34213.
92. Yeh, J. W., Recent progress in high entropyalloys. *European Journal of Control - EUR J CONTROL* **2006,** *31*, 633-648.
93. Kao, Y. F.; Chen, T. J.; Chen, S. K.; Yeh, J. W., *Journal of Alloys and Compounds* **2009,** *488* (1), 57-64.
94. Wang, X.; Guo, W.; Fu, Y., High entropyalloys: emerging materials for advanced functional applications. *Journal of Materials Chemistry A* **2021,** *9* (2), 663-701.
95. Jin, Z.; Lv, J.; Jia, H.; Liu, W.; Li, H.; Chen, Z.; Lin, X.; Xie, G.; Liu, X.; Sun, S.; Qiu, H.J., Nanoporous Al-Ni-Co-Ir-Mo High entropyAlloy for Record-High Water Splitting Activity in Acidic Environments. *Small* **2019,** *15* (47), 1904180.

96. Nguyen, T. X.; Liao, Y.C.; Lin, C.C.; Su, Y.-H.; Ting, J.M., Advanced High Entropy Perovskite Oxide Electrocatalyst for Oxygen Evolution Reaction. *Advanced Functional Materials* **2021,** *31* (27), 2101632.
97. Zhao, X.; Xue, Z.; Chen, W.; Bai, X.; Shi, R.; Mu, T., Ambient fast, large-scale synthesis of entropy-stabilized metal–organic framework nanosheets for electrocatalytic oxygen evolution. *Journal of Materials Chemistry A* **2019,** *7* (46), 26238-26242.
98. Dai, W.; Lu, T.; Pan, Y., Novel and promising electrocatalyst for oxygen evolution reaction based on MnFeCoNi high entropy alloy. *Journal of Power Sources* **2019,** *430*, 104-111.
99. Huang, J.; Wang, P.; Li, P.; Yin, H.; Wang, D., Regulating electrolytic Fe0.5CoNiCuZnx high entropy alloy electrodes for oxygen evolution reactions in alkaline solution. *Journal of Materials Science & Technology* **2021,** *93*, 110-118.
100. Tang, J.; Xu, J. L.; Ye, Z. G.; Li, X. B.; Luo, J. M., Microwave sintered porous CoCrFeNiMo high entropy alloy as an efficient electrocatalyst for alkaline oxygen evolution reaction. *Journal of Materials Science & Technology* **2021,** *79*, 171-177.
101. LH Liu, N. L., Mei Han, JR Han, HY Liang, Scalable synthesis of nanoporous high-entropy alloys for electrocatalytic oxygen evolution. *Rare Metals* **2021**.
102. Ding, Z.; Bian, J.; Shuang, S.; Liu, X.; Hu, Y.; Sun, C.; Yang, Y., High Entropy Intermetallic–Oxide Core–Shell Nanostructure as Superb Oxygen Evolution Reaction Catalyst. *Advanced Sustainable Systems* **2020,** *4* (5), 1900105.
103. Wang, D.; Liu, Z.; Du, S.; Zhang, Y.; Li, H.; Xiao, Z.; Chen, W.; Chen, R.; Wang, Y.; Zou, Y.; Wang, S., Low-temperature synthesis of small-sized high entropyoxides for water oxidation. *Journal of Materials Chemistry A* **2019,** *7* (42), 24211-24216.
104. Zhang, Y.; Dai, W.; Zhang, P.; Lu, T.; Pan, Y., In-situ electrochemical tuning of (CoNiMnZnFe)3O3.2 high entropyoxide for efficient oxygen evolution reactions. *Journal of Alloys and Compounds* **2021,** *868*, 159064.
105. Glasscott, M. W.; Pendergast, A. D.; Goines, S.; Bishop, A. R.; Hoang, A. T.; Renault, C.; Dick, J. E., Electrosynthesis of high entropymetallic glass nanoparticles for designer, multi-functional electrocatalysis. *Nat Commun* **2019,** *10* (1), 2650.

106. Yao, Y. *et al.* Carbothermal shock synthesis of high-entropy-alloy nanoparticles. *Science* **2018** vol. 359

107. Li, G., Blake, G. R. & Palstra, T. T. M. Vacancies in functional materials for clean energy storage and harvesting: the perfect imperfection. *Chem Soc Rev* **2017,** 46, 1693–1706.

108. Ede, S. R. & Luo, Z. Tuning the intrinsic catalytic activities of oxygen-evolution catalysts by doping: a comprehensive review. *Journal of Materials Chemistry A* **2021** 20131–20163, *9(36)*.

109. Smith, A., Mohs, A. & Nie, S. Tuning the optical and electronic properties of colloidal nanocrystals by lattice strain. *Nature Nanotech* **2009**, 4, 56–63.

110. Maiti, S., Maiti, K., Curnan, M. T., Kim, K., Noh, K.-J., & Han, J. W. Engineering electrocatalyst nanosurfaces to enrich the activity by inducing lattice strain. *Energy & Environmental Science* **2021**, *14*(7), 3717–3756.

111. Xia, Z., & Guo, S. Strain engineering of metal-based nanomaterials for energy electrocatalysis. *Chemical Society Reviews* **2019**, *48*(12), 3265–3278.

112. Liu, S., Shen, Y., Zhang, Y., Cui, B., Xi, S., Zhang, J., Xu, L., Zhu, S., Chen, Y., Deng, Y., Hu, W., Extreme Environmental Thermal Shock Induced Dislocation-Rich Pt Nanoparticles Boosting Hydrogen Evolution Reaction. *Adv. Mater.* **2022**, 34, 2106973.

113. Liu, S., Hu, Z., Wu, Y., Zhang, J., Zhang, Y., Cui, B., Liu, C., Hu, S., Zhao, N., Han, X., Cao, A., Chen, Y., Deng, Y., Hu, W., Dislocation-Strained IrNi Alloy Nanoparticles Driven by Thermal Shock for the Hydrogen Evolution Reaction. *Adv. Mater*. **2020**, 32, 2006034.

114. Zhuang, L., Ge, L., Yang, Y., Li, M., Jia, Y., Yao, X., Zhu, Z., *Adv. Mater.* **2017**, 29, 1606793.

Chapter 3

Experimental Methodology

In this chapter, the sample preparation process, the sample fabrication method, and the characterization strategies will be demonstrated. In addition, a brief introduction to the techniques and equipment will also be elaborated. The rapid and scalable laser-based process was used to fabricate multiple growth CoCuFeMnNi@CFP high-entropy alloys. The sample then was characterized by SEM, TEM, and XRD to reveal the surface morphology, crystal planes, and lattice structure. An LSV and EIS were prepared to evaluate the electrochemical OER performance.

3.1. Rationale for selection of synthetic method

To date, only limited methods have been possessed to downsize HEAs to the nanoscale.[1-3] A facile, two-step rapid laser irradiation (RLI) was chosen as the synthetic method, which is only room temperature and atmospheric pressure required. The 1064 nm I-laser can provide sufficient energy required with controllable patterns, power, irradiation rate and speed by an integrated user-friendly computer-aided design (EZ-CAD) program. The synthetic method takes advantage of well-established electrochemical equipment in laboratories and industries. Furthermore, versatility is highly recommendable since various transition metal, compounds, and hybrids can be further developed and synthesized.[4-6]

The selection of specific elements for the high-entropy alloy synthesis was based on several factors. Co, Cu, Fe, Mn, and Ni were chosen as they are all abundant, low-cost transition metals. These elements were also selected due to their favorable electrochemical properties, which are desirable for electrocatalysis applications. In addition, the selected elements have almost equal atomic radii, electronegativity, and valence electron concentrations, which can form a stable HEA system. *Cobalt* (Co) exhibits excellent catalytic activity and stability, particularly in oxygen evolution reactions (OER). It has a high electrical conductivity and can facilitate efficient electron transfer during electrochemical reactions. *Copper* (Cu) and *Nickel* (Ni) is widely recognized for theirs good conductivity and high catalytic activity in various electrochemical processes. *Iron* (Fe) and *Manganese* (Mn) capable of forming various oxidation states, which allows for a diverse range of redox reactions. These features are also predicted to improve the HEA electrocatalysts' stability and durability under demanding working conditions.

3.2. Synthesis

3.2.1. Preparation of Carbon-fiber-paper Substrate

Carbon fiber paper (CFP) (Toray, TGP-H-060, Suzhou Sinero Technology Co. Ltd.) is cut into 10 x 20 mm pieces for comfortable use and treated in 95% H_2SO_4 solution at 120^oC

for 6 hours to improve wettability, hydrophilic and enrich an oxygen-containing group of CFP.[7] Then, the CFP is cleaned by standard 95% ethanol, deionized water (DIW) process before dried in an oven at 60°C.

3.2.2. Preparation of Metal Precursor Solution

Cobalt(II) nitrate hexahydrate ($Co(NO_3)_2.6H_2O$), copper(II) nitrate trihydrate ($Cu(NO_3)_2.3H_2O$), iron(III) nitrate nonahydrate ($Fe(NO_3)_3.9H_2O$), manganese(II) nitrate hydrate ($Mn(NO_3)_2.H_2O$), nickel(II) nitrate hexahydrate ($Ni(NO_3)_2.6H_2O$) purchased from Sigma Aldrich Chemistry are mixed in ethanol-based solution with 10 mmol/L for each element. In general, an ethanol-based solution results in improved wettability and uniform loading to the carbon paper substrate. The mixed solution was directly dropped onto CFP with a loading of ~120 µL/cm^2 and left to dry at room temperature.

3.2.3. Rapid Laser Irradiation (RLI)

3.2.3.1. Synthesis of pristine CoCuFeMnNi@CFP HEAs NPs

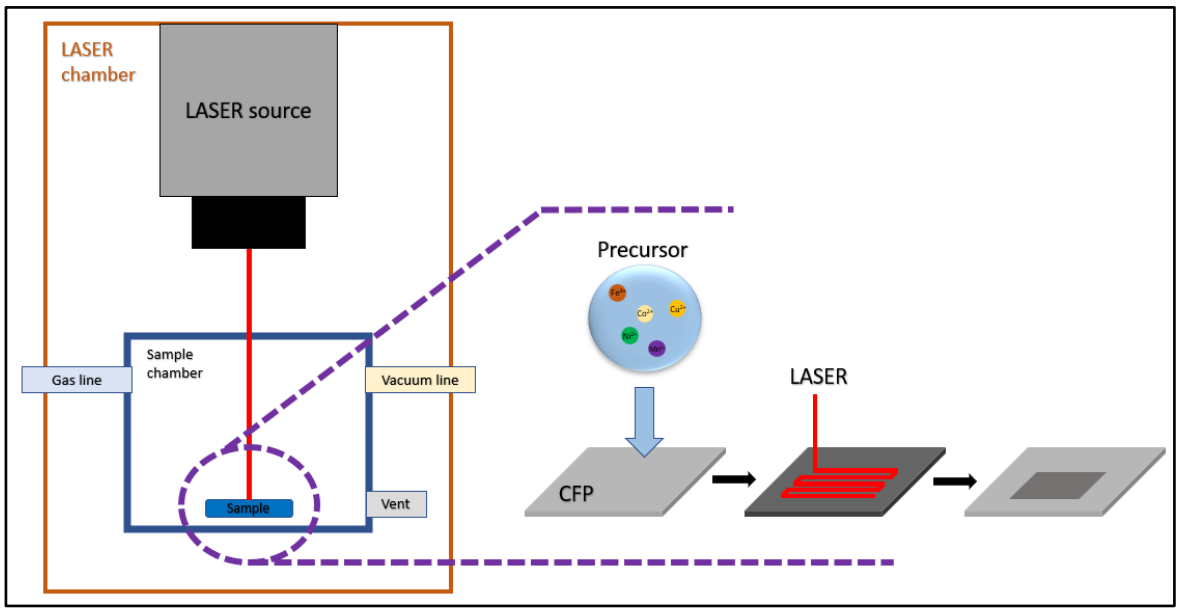

Figure 3.1: Schematic diagram of RLI process.

The RLI process is achieved by directly irradiating the samples under a commercial laser source (JPT-M7-100W). **Figure 3.1** illustrates the RLI process, in which the samples were placed in a chamber, protected by the anti-IR-UV glass for the safety of users. The chamber can be vacuumed or filled with inert gas depending on the purpose of fabrication. The laser is set to 30 µm beam spot size at the focus point and 30 µm line space for uniform irradiation. The irradiation area was 5 mm x 5 mm square, simultaneously scanned by a 1064 nm pulsed laser beam with the frequency of 900 kHz in 2 ns pulse width and scanning speed of 40 mm/s. The sample was then rinsed by standard ethanol and DI water multiple times and followed by drying at 60^{o}C in the oven.

3.2.3.2. Post-synthesis laser continuous irradiation treatment

The laser parameters and lens position are set to the continuous mode by setting the frequency and pulsed width value to 1. The effect of laser treatment is investigated by the different output power of 1 W, 2 W, 4 W, and 8 W. Irradiation speed is also an important factor. The beam spot size and line space remain unchanged. The HEA NPs sample was irradiated on all the fabricated areas. After treatment, the sample was rinsed with standard ethanol and DI water multiple times and followed by natural drying at room temperature.

3.3. Characterization and Testing Techniques

3.3.1. X-ray Diffraction (XRD)

X-ray diffractometer (XRD Bruker D8 Advance) was used to characterize the structure and phase of the sample using Cu Kα_1 radiation running at 40 kV and 40 mA. The samples were scanned in the range of $30° \leq 2\theta \leq 100°$ in Bragg-Brentano geometry.

The X-ray diffractometer contains four major parts including the X-ray source, system optics, sample stage, and the detector. The x-ray source is usually a cathode tube which applies high voltage to expel electrons to bombard the target copper material. Characteristic x-ray Cu Kα is generated and filtered by a set of monochromators and slits. Then the

monochromatic x-ray finally reaches the sample surface. The interference then creates the diffraction pattern of the sample, which follows Bragg's law:

$$n\lambda = 2dsin\theta$$

where n refers to the order of reflection, λ is the wavelength of the x-ray, d presents the spacing between diffracting planes, and θ is the diffraction angle. The Bragg-Brentano geometry is able to provide spectrums with high resolution and intensity nonetheless careful and accurate sample alignment are satisfied.

A thin film X-ray diffractometer (D8 Advance Bruker) is employed to get the diffraction pattern of MG HEA CoCuFeMnNi after treatment using Cu $K\alpha_1$ (40 kV, 30 mA, 1.540598 Å wavelength). The samples should be scanned 2-theta from $30° \; to \; 90°$ with a $0.02°$ step size and X-ray grazing angle of 1.0°.

3.3.2. Scanning Electron Microscopy (SEM)

In this work, a field-emission scanning electron microscope (FE-SEM 7600F, JEOL, JP) at 5 kV accelerating voltage was used to characterize the surface morphology and analyse the chemical composition of the sample. The SEM's main components are an electron gun, electromagnetic lens, sample chamber, and detectors. All the components are placed under a high vacuum to ensure a non-scattering environment and free mean path of electrons from the gun towards the sample surface. The electron beam from the source filament is accelerated and focused by a set of beam correction components and an electromagnetic lens (Wehnelt cap, objective aperture, condenser lens, scanning coils, and objective lens). The primary electron beam then interacts with the surface of the specimen, generating various signals including secondary electrons (SEs), backscattered electrons (BEs), the characteristic x-rays. Each of these signals will be collected by a specific detector and then demonstrates to an output device. The SEs, which are generated from inelastic scattering events of the primary electrons with electrons within the atoms of the sample, usually have the low energy levels and can only escape from a few nanometers below the specimen surface. Therefore, SEs images can accurately show the surface information, such as the

morphology and topology of the sample. On the other hand, the BEs generated from elastic scattering, will provide atomic mass contrast images. Besides, the characteristic x-rays are generated when an electron at a higher energy level moves to replace a lower energy level electron that was knocked out by a primary electron. The energy of the x-ray is characteristic of the chemical element. The energy dispersive x-ray spectroscopy (EDS) mode in SEM can qualitatively analyze the different elements present in the sample from emitted characteristic x-ray.

3.3.3. Transmission Electron Microscopy (TEM)

To prepare the synthesized HEA sample for TEM, the carbon paper sample was dipped in 02 mL DI water, followed by 30 minutes in an ultrasonication bath. After that, the solution was carefully dropped onto the carbon-coated copper grid and dried at room temperature. It is important to ensure the sample is protected from any contaminants during drying. The sample was then ready to be mounted onto the TEM holder.

A high-resolution transmission electron microscope (HRTEM JEM-2100F, JEOL, JP) at 200 kV accelerating voltage was mainly utilized to capture atomic-resolution images of the HEAs for crystallinity and lattice structures. The electron beam is generated by the electron gun and accelerated by 200 kV. After which the beam is adjusted to parallel by the condenser lens before interacting with the specimen. All the signals afterward will be focused on the back focal plane of the objective lens, forming the primary beam. This primary beam will be captured by the fluorescent screen or electronic detector after going through the set of electromagnetic lenses including the intermediate lens and projector lens as shown in **Figure 3.2**. Various collection modes, such as bright-field (BF), annular dark-field (ADF), high-angle annular dark-field (HAADF), are angle-dependent and can be used to selectively extract specific information from the scattered electrons.

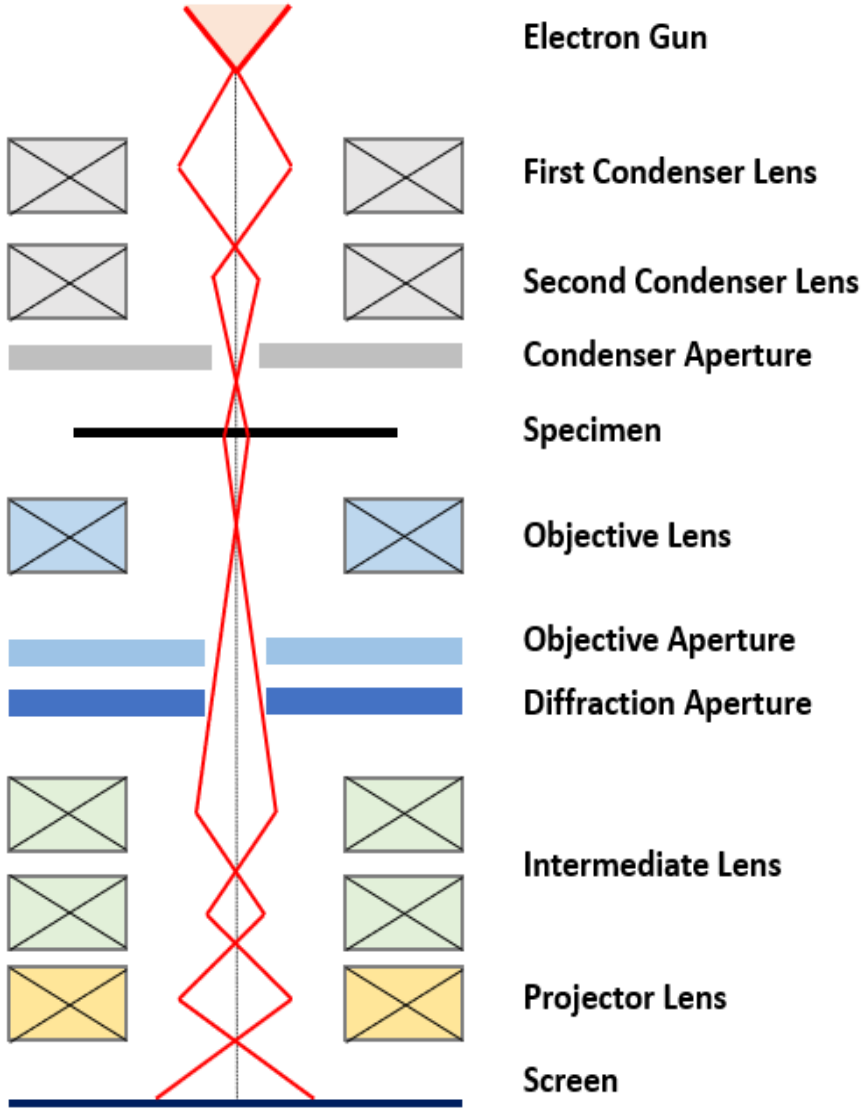

Figure 3.2: Schematic structure of TEM.

3.3.4. Electrochemical Characterization

All electrochemical measurements were carried out on a glass cell with a three-electrode system connected to a workstation (PGSTAT302N, Metrohm Autolab, Netherlands) as shown in **Figure 3.3**. The prepared sample with CFP substate served as the working electrode, while the counter electrode was a high purity carbon electrode and a saturated Ag/AgCl reference electrode. 1 M KOH (pH = 14) was used as the electrolyte. The potential measured versus Ag/AgCl reference electrode will be converted to potential versus RHE through the equation as follow:[9]

$$E_{RHE} = E_{Ag/AgCl} + 0.059 \times pH + 0.197$$

Figure 3.3: Photo of the three-electrode system and PGSTAT302N workstation.

3.3.4.1. Linear Sweep Voltammetry (LSV)

LSV is a simple electrochemical technique which measures the potential between the working electrode and the reference electrode, while measuring the current at the counter electrode. Then the potential is plotted against the current for a linear voltammogram. The scanning rate was set to 5 mV/s from 0 to 0.7 V with a potential step of 0.00244 V. All LSV measurement is compensated by iR-compensation.

3.3.4.2. Electrochemical Impedance Spectroscopy (EIS)

EIS is used to investigate the electrochemical characteristic of an electrochemical cell including the resistance of solution, charge transfer resistance, polarization, and capacitance by simply applying an AC potential. In this work, the three-electrode system needs to consider the Simplified Randles Cell (SRC) to characterize the electrolyte resistance, the double-layer capacitance, and the charge transfer resistance. The equivalent circuit for the SRC is demonstrated in **Figure 3.4**.

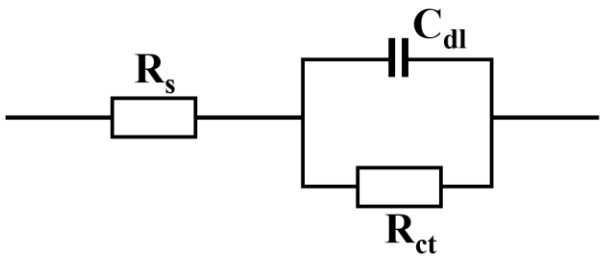

Figure 3.4: Simple Randle Cell equivalent circuit

Solution resistance (R_s) or electrolyte resistance or is an important factor in the impedance of the electrochemical cell. Accurate LSV measurement from the three-electrode system needs to compensate for the solution resistance between electrodes. The electrolyte resistance of ionic solution is influenced by the concentration and type of ions, temperature, and geometry of the area. Fortunately, the solution resistance can be obtained by fitting EIS data from the Nyquist plot.

The interface between the surrounding electrolyte and an electrode will form an electrical double layer. The charged ions are separated from the charged electrode by an insulating space, which behaves like a capacitor. The double layer capacitance (C_{dl}) is affected by the interface temperature, electrode potential, ionic concentration, roughness, an oxide layer, etc.[10]

The charge transfer resistance, which is kinetically controlled by an electrochemical reaction, occurs when the metal ions diffuse into the electrolyte after receiving electrons. When the overpotential is very small and the electrochemical system reaches equilibrium, the charge transfer resistance can be expressed to:

$$R_{ct} = \frac{RT}{nFi}$$

where R refers to gas constant, T is temperature, F presents Faraday constant, n is the number of electrons involved, and i is the exchange current density.

3.3.4.3. Electrochemical active surface area (ECSA)

The area of the electrode that is available for electrochemical reaction to occur, by reactants or products in the electrolyte of the electrochemical cell, is called electrochemical active surface area (ECSA). It is an important parameter in electrochemical systems such as batteries, fuel cells, sensors, etc. The ECSA of an electrocatalyst electrode can be calculated using the equation:

$$ECSA = \frac{C_{dl}}{C_s}$$

where C_{dl} is the double-layer capacitance, C_s is the volumetric capacitance, specified as 40 μFcm^{-2} in 1 M KOH alkaline electrolyte. C_{dl} in the three-electrode model can be measured using the cyclic voltammetry technique. The potential of the working electrode is swept at a constant rate, while the current is recorded. Then C_{dl} is calculated by measuring the change in current (ΔJ) respectively to the change in potential (ΔE) at the double-layer capacitive charging and discharging, typically at low potentials:

$$C_{dl} = \frac{\Delta J}{\Delta E}$$

References

1. Wang, X.; Guo, W.; Fu, Y., High-entropy alloys: emerging materials for advanced functional applications. *Journal of Materials Chemistry A* **2021,** *9* (2), 663-701.
2. Ye, Y. F.; Wang, Q.; Lu, J.; Liu, C. T.; Yang, Y., High-entropy alloy: challenges and prospects. *Materials Today* **2016,** *19* (6), 349-362.
3. Miracle, D. B.; Senkov, O. N., A critical review of high entropy alloys and related concepts. *Acta Materialia* **2017,** *122*, 448-511.
4. Lu, Y.; Huang, K.; Cao, X.; Zhang, L.; Wang, T.; Peng, D.; Zhang, B.; Liu, Z.; Wu, J.; Zhang, Y.; Chen, C.; Huang, Y., Atomically Dispersed Intrinsic Hollow Sites of M-M1-M (M1 = Pt, Ir; M = Fe, Co, Ni, Cu, Pt, Ir) on FeCoNiCuPtIr Nanocrystals Enabling Rapid Water Redox. *Advanced Functional Materials* **2022,** *n/a* (n/a), 2110645.
5. Yao, Y.; Huang, Z.; Xie, P.; Lacey Steven, D.; Jacob Rohit, J.; Xie, H.; Chen, F.; Nie, A.; Pu, T.; Rehwoldt, M.; Yu, D.; Zachariah Michael, R.; Wang, C.; Shahbazian-Yassar, R.; Li, J.; Hu, L., Carbothermal shock synthesis of high-entropy-alloy nanoparticles. *Science* **2018,** *359* (6383), 1489-1494.
6. Waag, F.; Li, Y.; Ziefuß, A. R.; Bertin, E.; Kamp, M.; Duppel, V.; Marzun, G.; Kienle, L.; Barcikowski, S.; Gökce, B., Kinetically-controlled laser-synthesis of colloidal high-entropy alloy nanoparticles. *RSC Advances* **2019,** *9* (32), 18547-18558.
7. Sorokin, A. E.; Petrova, G. N.; Donskikh, I. N., Use of Chemical and Electrochemical Treatment Methods in the Liquid-Phase Modification of Carbon Fiber and Fiberglass Surfaces in the Production of Construction Materials: A Review. *Theoretical Foundations of Chemical Engineering* **2020,** *54* (5), 1061-1067.
8. Marturi, N., Vision and visual servoing for nanomanipulation and nanocharacterization in scanning electron microscope. **2013**.
9. S., B. V., *Fundamentals of Electrochemistry*. Wiley: 2005; Vol. 44.
10. Lorena, B.; Marcus, P.; Christos, V.; Andrea, H. In *Smart cements: repairs and sensors for concrete assets*, Proc.SPIE, 2018.

Chapter 4

CoCuFeMnNi@CFP high-entropy alloy nanoparticles synthesis and characterization

This chapter demonstrates the results of high-entropy alloy nanoparticles CoCuFeMnNi@CFP fabrication, including physical and electrochemical characterization. The CoCuFeMnNi@CFP HEA NPs surface morphology, element composition, crystal phase, and lattice structure will be revealed and analyzed. In addition, electrochemical tests including Linear Sweep Voltammetry, Electrochemical Impedance Spectroscopy and the relationship between physical and electrochemical properties will also be discussed.

4.1. Rapid laser irradiation in the synthesis of CoCuFeMnNi@CFP high-entropy alloy nanoparticles.

Carbon-fiber papers (CFP) (Toray, TGP-H-060, Suzhou Sinero Technology Co. Ltd.) are cut into 10 x 20 mm pieces for comfortable use and treated in 95% H_2SO_4 solution at 120°C for 6 hours to improve wettability, hydrophilic and enrich an oxygen-containing group of CFP.[7] Then, the CFP is cleaned by standard 95% ethanol, deionized water (DIW) process before drying in an oven at 60°C. Cobalt(II) nitrate hexahydrate ($Co(NO_3)_2.6H_2O$), copper(II) nitrate trihydrate ($Cu(NO_3)_2.3H_2O$), iron(III) nitrate nonahydrate ($Fe(NO_3)_3.9H_2O$), manganese(II) nitrate hydrate ($Mn(NO_3)_2.H_2O$), nickel(II) nitrate hexahydrate ($Ni(NO_3)_2.6H_2O$) purchased from Sigma Aldrich Chemistry are mixed in ethanol-based solution with different concentration (2 mM, 5 mM, and 10 mM) for each element (Co:Cu:Fe:Mn:Ni = 1:1:1:1:1). In general, an ethanol-based solution results in improved wettability and uniform loading to the carbon paper substrate. The mixed solution was directly dropped onto CFP with a loading of ~40 µL/cm^2 and left to dry at room temperature. Therefore, the CFP was coated with a layer of salt metal and then placed into an inert-gas chamber. Followed by a set of laser irradiation processes, the mentioned mixed metal precursor was decomposed and formed HEAs nanoparticles that distribute all around the carbon fiber was shown in **Figure 4.1**.

Table 4.1: Parameters of laser irradiation for synthesis HEA NPs

Power (W)	Speed (mm/s)	Frequency (kHz)	Pulse width (ns)	Line space (mm)	Spot size (mm)
4	40	900	2	0.03	0.03

The RLI method, which specific parameters shown in **Table 4.1**, results in a uniform dispersion of HEA CoCuFeMnNi nanoparticles on the carbon fiber base. The interaction of the laser with the materials in the precursor is mostly described as photon-induced electronic excitation absorption. Electrons in the irradiated substrates absorb incident laser energy and quickly transmit the absorbed energy to atoms via strong collisions, causing the substrate temperature to rise. When the surface temperature of an irradiated substrate rises

to melting or even vaporization temperatures, the substrate will change from solid to liquid or gas. In pulse mode, the rapid heating and rapid quenching result in the formation of nanoparticles. **Figure 4.1a-b** show the change on the surface of carbon fiber before and after fabrication, with the integrity of the carbon fiber maintained.

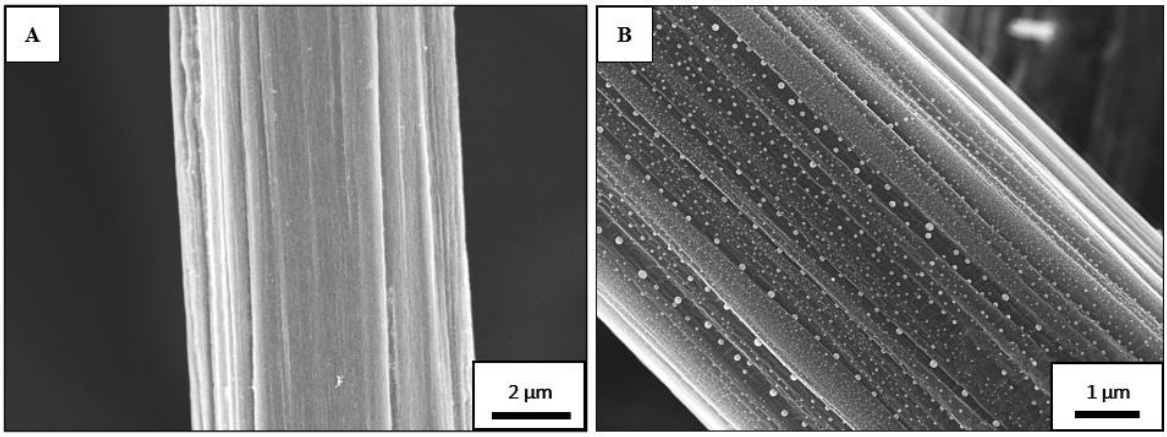

Figure 4.1: FESEM images of the sample: (a) Pristine carbon fiber, (b) After fabrication

4.2. Physical Characterization

4.2.1. Morphology and Particle Size

The morphology of the HEA nanoparticle prepared on different precursor concentrations was investigated. **Figure 4.2 to 4.4** demonstrate the FESEM images with the particle size distribution plots of the CoCuFeMnNi@CFP HEAs synthesized by 2 mM, 5 mM, and 10mM each element concentration precursors, respectively. The high magnification images show partially spherical nanoparticles are embedded on the surface of the carbon fiber. The lower concentration sample results in a smaller particle size and higher particle density. For the 2 mM sample, the HEA NPs uniformly distributed on the surface of the carbon fiber, present almost identically in a spherical shape with an average diameter of 10.04 ± 1.39 nm (**Figure 4.2**). The 5 mM sample shows some particles over 50 nm in size despite having an average diameter of 21.03 ± 1.59 nm as shown in **Figure 4.3**. This might be explained by the anomaly on the carbon fiber surface at a particular area which results in a wider range of particle density. **Figure 4.4** shows that NPs synthesized by 10 mM

precursor have non-uniform distribution with a particle size ranging from 30 to 300 nm at an average diameter of 148.24 ± 6.76 nm. The larger particles also result in a spacious surface as particle density is only about 3.6 – 10.4 particles per micrometer square (**Table 4.2**).

Table 4.2: Summary of particle size and density related to precursor concentration.

Sample	Particle size (nm)	Particle density (particles per μm^2)
2 mM	10.04 ± 1.39	232.2 ~ 290.8
5 mM	21.03 ± 1.59	78.4 ~ 162.7
10 mM	148.24 ± 6.76	3.6 ~ 10.4

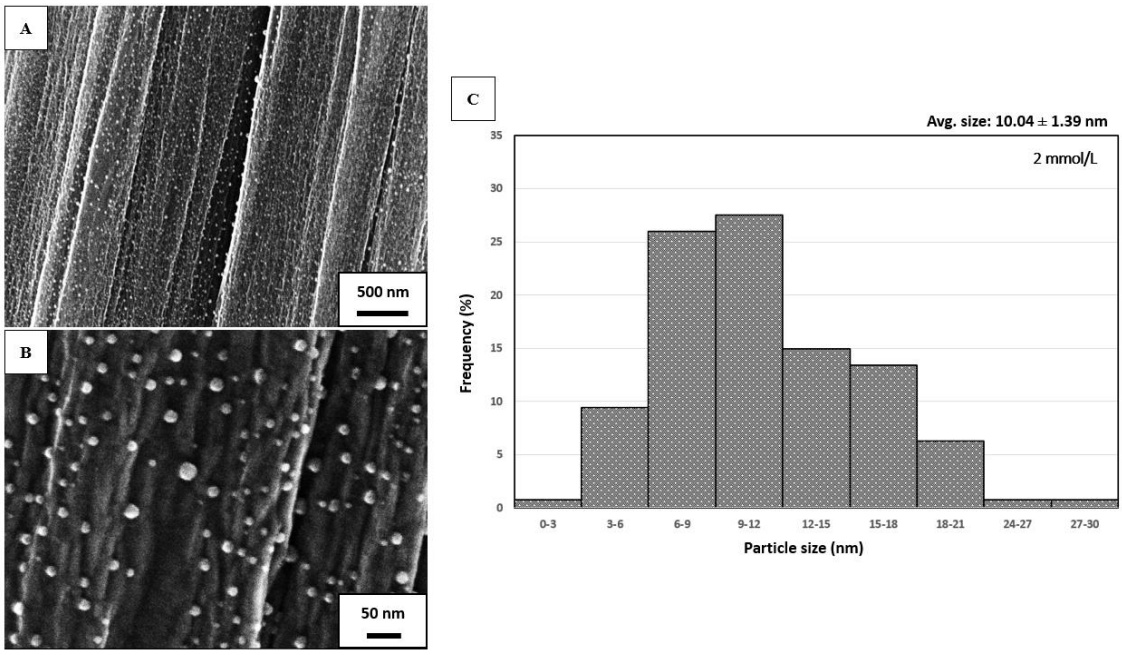

Figure 4.2: Morphology of CoCuFeMnNi@CFP HEAs NPs synthesized by 2 mM precursor: (a-b) Low and high magnification FESEM images, (c) Plot of particle size distribution

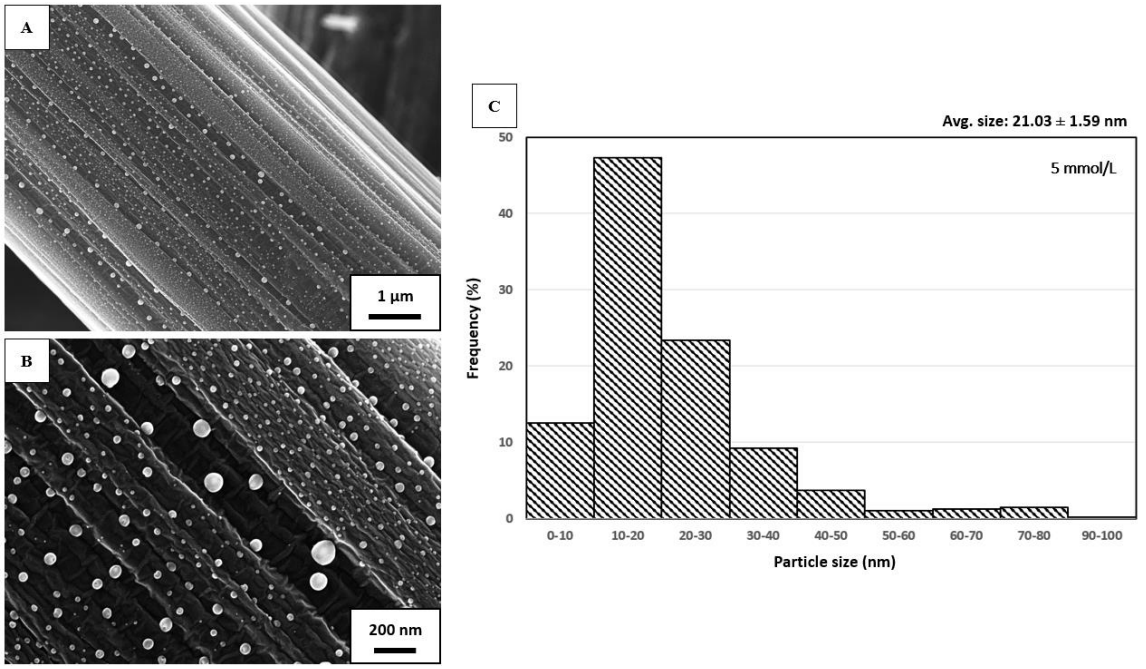

Figure 4.3: Morphology of CoCuFeMnNi@CFP HEAs NPs synthesized by 5 mM precursor: (a-b) Low and high magnification FESEM images, (c) Plot of particle size distribution

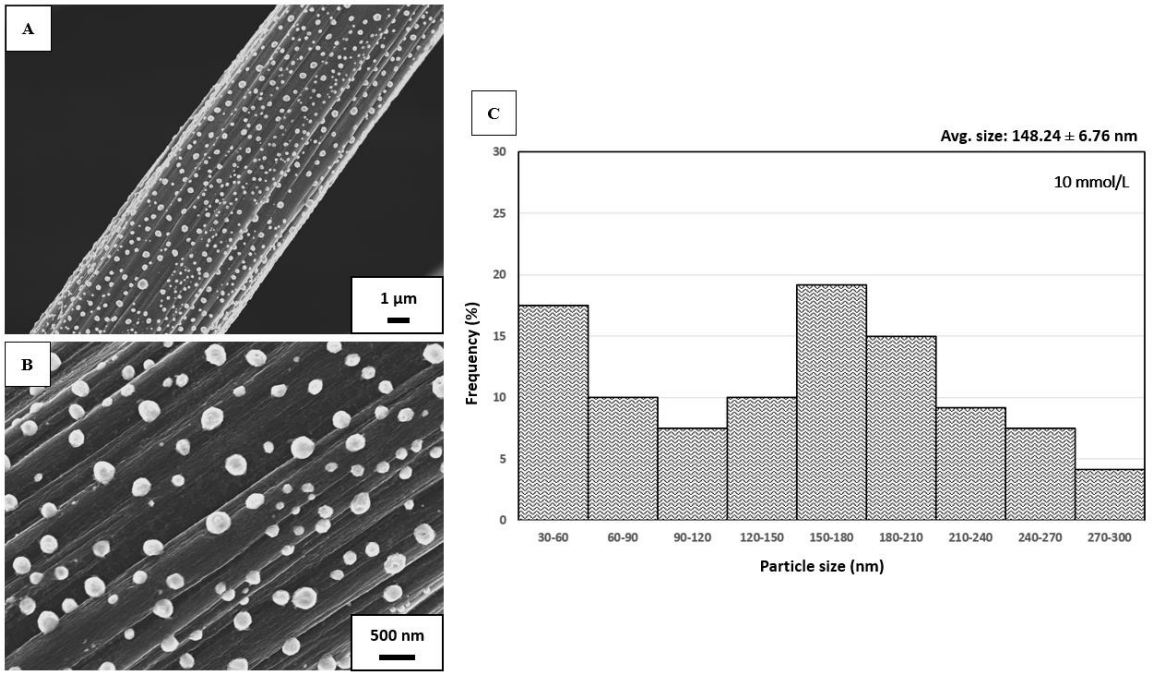

Figure 4.4: Morphology of CoCuFeMnNi@CFP HEAs NPs synthesized by 10 mM precursor: (a-b) Low and high magnification FESEM images, (c) Plot of particle size distribution

4.2.2. Elemental Compositions and Structures

The element composition was analyzed by STEM-EDS. The characteristic X-ray emission peaks and the corresponding elements map as shown in **Figure 4.5**. Excluding the domination of carbon signal from the carbon fiber substrate, the presence of 5 transitional metals (Co, Cu, Fe, Mn, Ni) was confirmed as they are distributed across one single nanoparticle as illustrated in **Figure 4.6**.

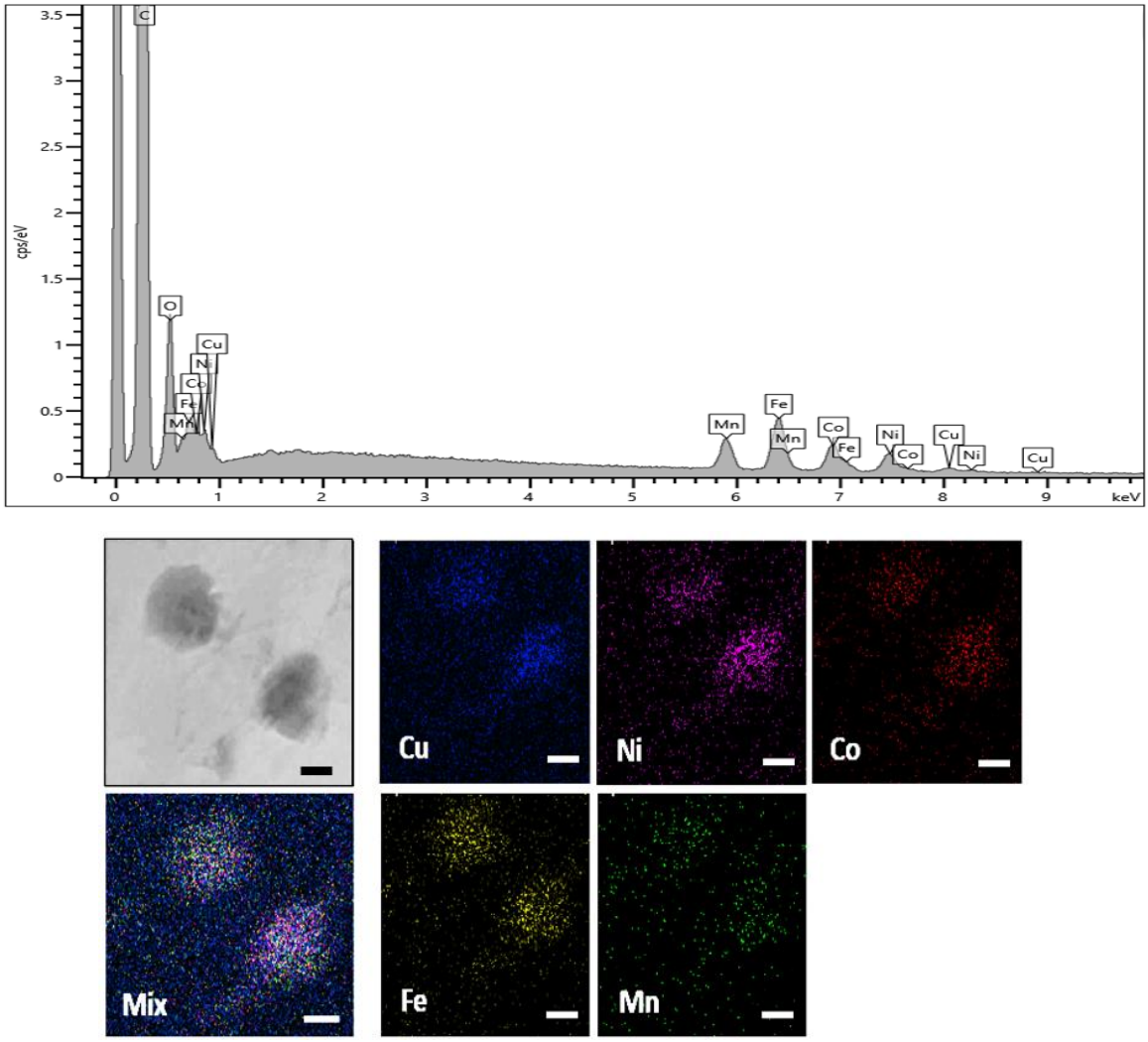

Figure 4.5: EDX spectrum and element mapping images of the quinary high-entropy alloy particles, the scale bar indicates 10 nm.

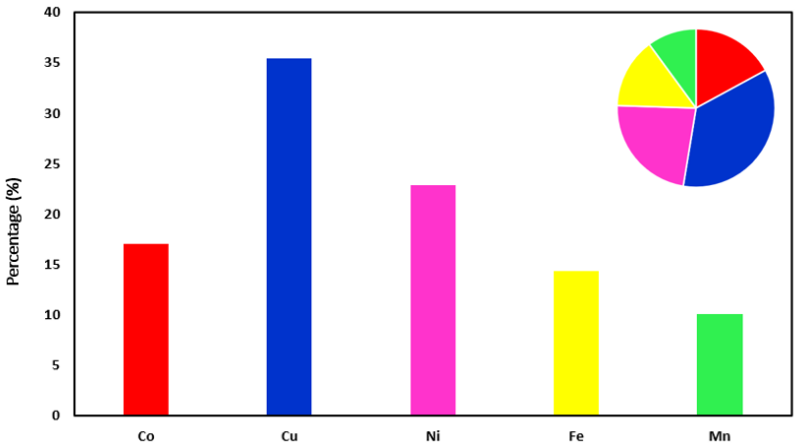

Figure 4.6: Elements content distribution of the HEAs.

Table 4.3: Elements weight ratio of the sample.

Elements	**Weight (%)**
Co	17.1
Cu	34.8
Fe	14.4
Mn	10.8
Ni	22.9

Equation 4.1: Mixing Gibbs Free Energy equation:

$$\Delta G_{mix} = \Delta H_{mix} - T\Delta S_{mix}$$

The atomic weight distribution ratios are demonstrated in **Table 4.3**. The result suggests that the HEA consists of Co (17.1%), Cu (34.8%), Fe (14.4%), Mn (10.8%), Ni (22.9%). The differences in atomic size, electronegativity, affinity, valence electron concentration, etc… can influence the potential of element bonding preferences and result in weight ratio distribution. It was reported that the formation of multi-element solid solution requires the following conditions: $\delta \leq 6.6\%$; $-11.6 < \Delta H_{mix} < 3.2$ (kJ.mol^{-1}), where δ is the average atomic radius difference and ΔH_{mix} is the mixing enthalpy.[1] In this work, the atomic radius difference is δ = 3.3%, the mixing enthalpy ΔH_{mix} = 1.13 kJ.mol^{-1}, the corresponding mixing entropy ΔS_{mix} = 12.65 J.K^{-1}.mol^{-1}. The Gibbs free energy of mixing ΔG_{mix} at room temperature (298 K) according to **Equation 4.1** is -2.64 kJ.mol^{-1}.

The structure and phase composition of the synthesized HEA were analysed by XRD D8 Bruker Advance. **Figure 4.7** indicates the diffraction peaks at 2-theta equals 43.25° and 74.05° (red), which correspond to (111) and (220) crystal planes of a single-phase face-centered cubic lattice structure of $Co_{0.2}Cu_{0.2}Fe_{0.2}Mn_{0.2}Ni_{0.2}$ (JCPDS No. 04-024-9060). The d-spacing of the (111) and (220) planes are 2.090 Å and 1.279 Å. The dominating peak at around 54.5° (green) corresponded to the carbon (JCPDS No. 00-056-1059), which was from the carbon fiber substrate. This result confirmed the feasibility of the RLI method to synthesize the HEA structures that grow upon a carbon-based substrate.

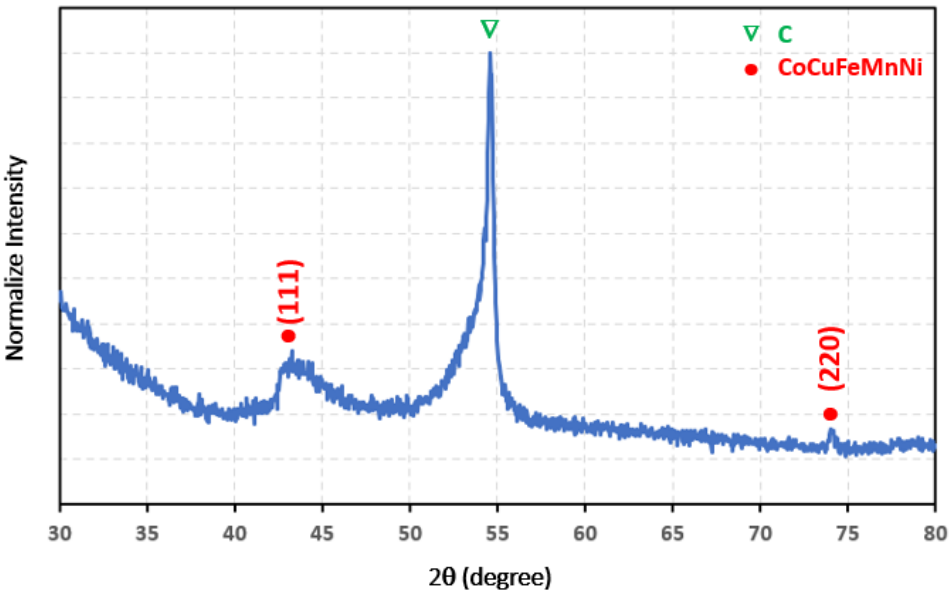

Figure 4.7: X-ray diffraction pattern of HEA CoCuFeMnNi@CFPx`

Figure 4.8 shows the HRTEM image of the sample along with the structure, crystal planes, and the lattice spacing was measured by processing fast Fourier transformation (FFT). The dispersion of HEA nanoparticles across a carbon fiber at low magnification is shown in **Figure 4.8a**. Two representative HEA NPs named particle A (**Figure 4.8b**) and particle B (**Figure 4.8e**) were investigated. **Figure 4.8c-d** shows the high-resolution image of particle A and its FFT pattern taken at zone axis [1 0 1], which illustrates the face-centered cubic (FCC) lattice with the twining plane of (0 2 0) sharing the <1 1 1> boundary. Particle B magnified crystal lattice image as shown in **Figure 4.8f** also indicates a single-phase FCC crystal structure and the FFT pattern (**Figure 4.8g**) taken along the [1 1 1] orientation has confirmed the face-centered cubic crystalline structure and its corresponding crystal planes. These results confirmed the structures from the previous XRD pattern. The absence of intermetallic formation or phase separation might be explained by the rapid quenching nucleation process, which directly formed solid-solution nanoparticles.[2-4] **Figure 4.8h-j**. show no dislocation in the atomic lattice of particle B along the (0 -2 2), (-2 2 0), and (-2 0 2) lattice plane, respectively. Except for a small stacking fault in the (0 -2 2) plane, marked by a red curve line. The d-spacing along the planes measured through inverse FFT processed image as 1.29 Å, which corresponds to the (2 2 0) lattice plane identified previously in the XRD pattern.

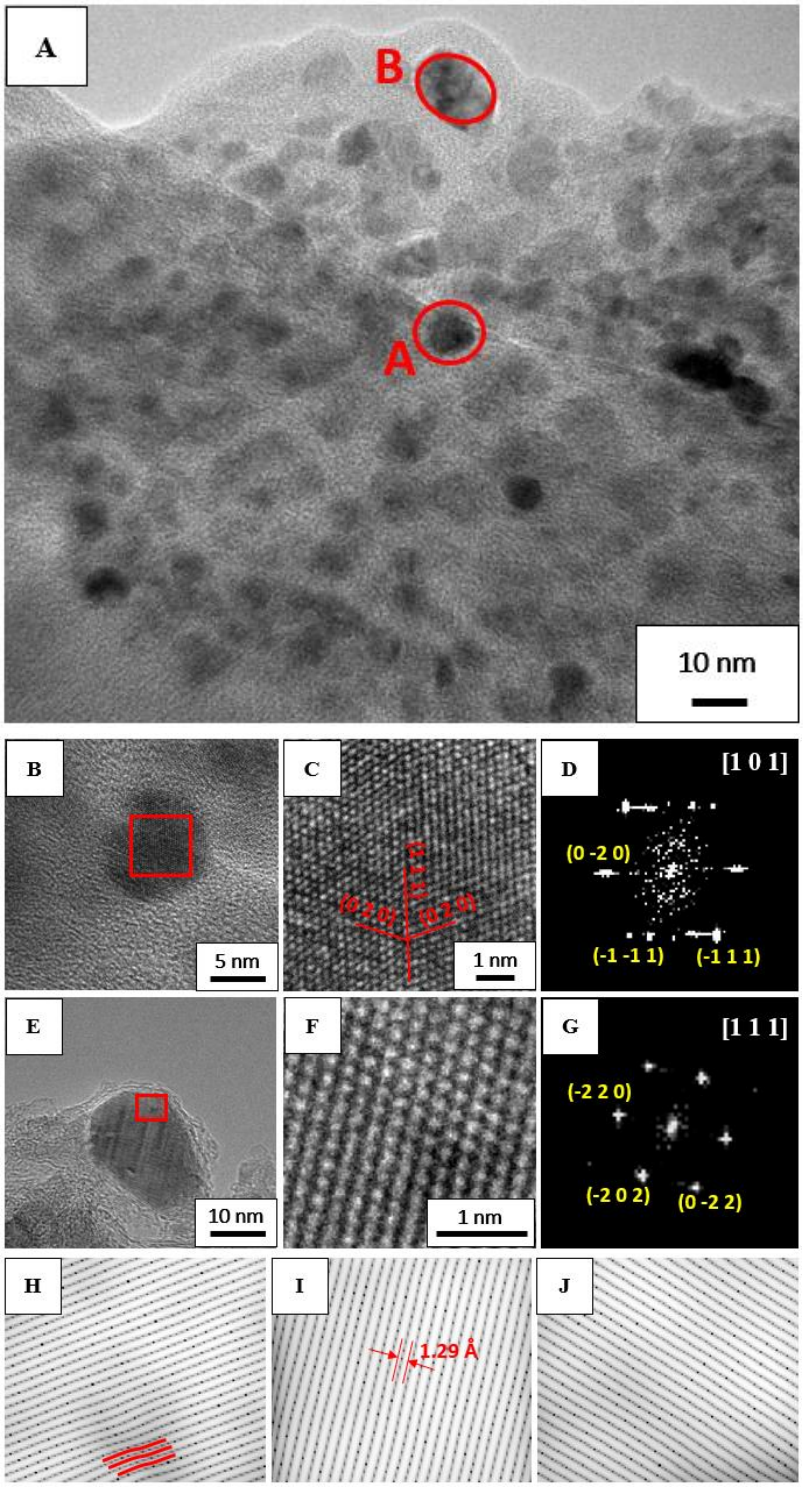

Figure 4.8: (a) low magnification bright-field HRTEM image, (b-d) high magnification images and FFT pattern of particle A, (e-g) high magnification images and FFT pattern of particle B, (h-j) IFFT transformed images along (0 -2 2), (-2 2 0), and (-2 0 2) lattice plane of particle B, respectively.

4.3. Electrocatalytic OER Performance

Figure 4.9 shows the electrochemical tests of the fabricated HEA CoCuFeMnNi@CFP and the comparison between three different precursor concentration samples: CoCuFeMnNi at 2 mmol/L (CoCuFeMnNi-2mM), at 5 mmol/L (CoCuFeMnNi-5mM), and 10 mmol/L (CoCuFeMnNi-10mM). Oxygen evolution reactions were conducted in 1M KOH electrolyte through a standard three-electrode system with the scanning rate set to 5 mV/s from an external voltage range of 0 to 0.7 V with a potential step of 0.00244 V. **Figure 4.9a** and **Figure 4.9b** show the catalytic activities for OER in LSV curves and the overpotential at a current density of 10 $mAcm^{-2}$ of three samples. The results indicate the CoCuFeMnNi-2mM sample, which has the smallest average particle size, exhibited better OER activity in comparison to the other two. Especially, the CoCuFeMnNi-2mM sample reached the overpotential of 330 mV at a current density of 10 $mAcm^{-2}$, which is 14 mV and 38 mV lower than the 5mM sample (344 mV) and 10mM sample (368 mV), respectively.

To elucidate the mechanism under the catalytic behaviors, the Tafel slopes of 3 samples were calculated, as shown in **Figure 4.9c**. The electron transfer at the electrode and electrolyte interface is faster with a smaller Tafel slope. The Tafel slopes for 2 mM, 5 mM, and 10 mM HEA CoCuFeMnNi are 79.6, 81.7, and 91.8 $mVdec^{-1}$ respectively. The 2 mM sample of CoCuFeMnNi HEA NPs exhibited the least Tafel slope, which agreed with the dominant OER performance as compared to other samples. The charge transfer behavior occurring at the interface between the catalyst and the electrolyte is also important to the electrocatalyst performance. Therefore, the electrochemical impedance spectroscopy (EIS) was performed at the operating voltage of 1.55 V vs. RHE then the Nyquist plot was displayed in **Figure 4.9d**. The SRC equivalent circuit (**Figure 4.9d** inset) was confirmed and fitted in NOVA (Metrohm Autolab) software, which indicated the contribution of electrolyte resistance (R_s), charge transfer resistance (R_{ct}), and the double layer capacitance (C_{dl}). The CoCuFeMnNi-10mM showed the largest semicircle that represented the R_{ct} = 114 Ω at a very low frequency. Other samples showed smaller semicircles of Nyquist plots that indicated R_{ct} = 25.8 and 52.0 Ω respectively for 2 mM and 5 mM samples. It is worth

noting that the smaller precursor concentration samples result in smaller nanoparticles. For a spherical particle, the surface area to volume ratio is inversely proportional to the radius of the particle. This means more surface area will be exposed to reaction for smaller particles and vice versa. Therefore, the 10 mM sample, which has an average particle size of over 100 nm, would find more challenges to make electrode-electrolyte charge transfer for thermodynamic catalysis.

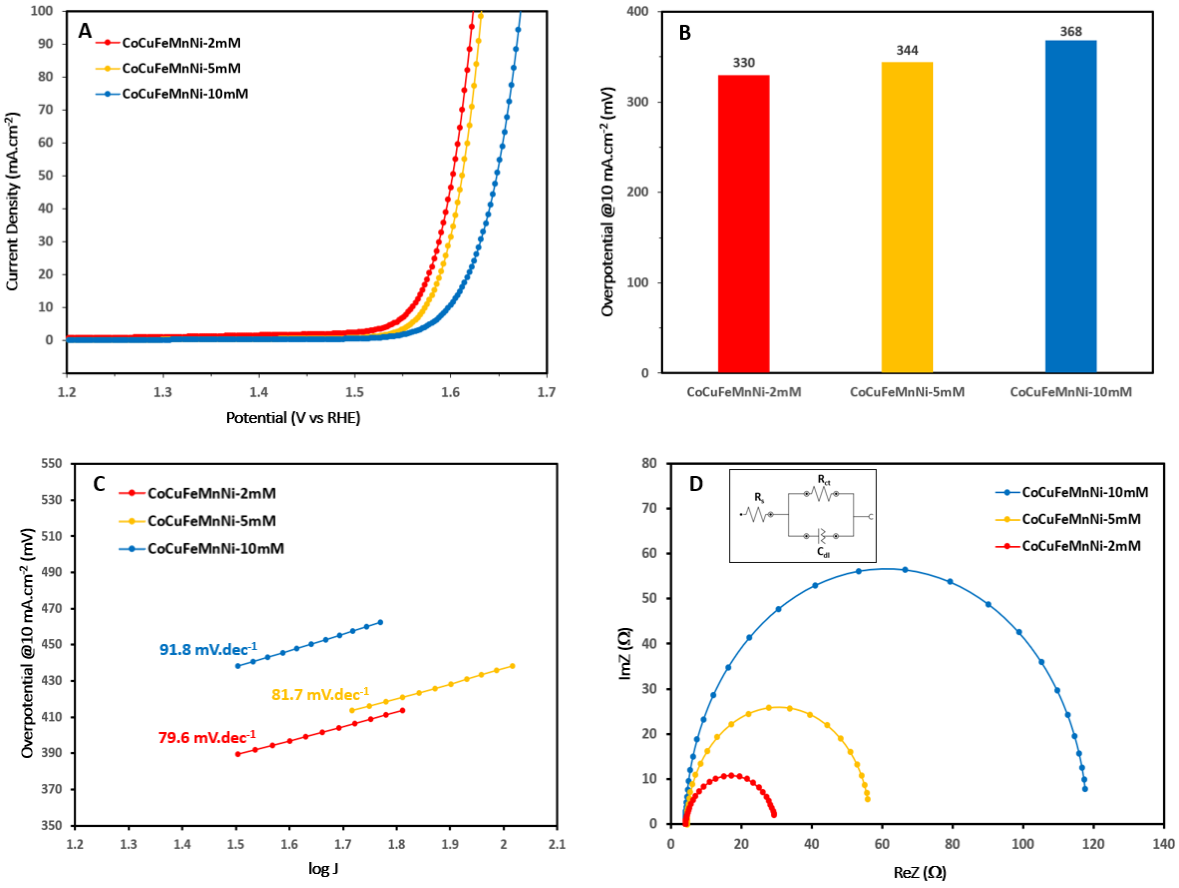

Figure 4.9: a) LSV curve, b) Overpotential at a current density of 10 mA.cm^{-2}, c) Tafel plot, and d) EIS plot with equivalent circuit (inset) for different precursor concentration growth of CoCuFeMnNi high-entropy alloy nanoparticles.

4.4. Conclusions

In summary, the rapid laser irradiation method has successfully fabricated high-entropy alloy nanoparticles of non-noble metal with particle diameters ranging from ten to hundreds of nanometers, which depends on the precursor concentration. The morphology and crystallography have been studied to show the uniform distribution of nanoparticles across the surface of carbon fiber, the element composition and phase of the high-entropy alloys, and the well-oriented face-centered cubic crystal structure, supported by the XRD, SEM, TEM, and EDS results. The fabricated HEAs electrocatalysts have shown a trend that smaller nanoparticles with high particle density resulted in larger surface area and more active sites, which provide better OER performance. Therefore, The CoCuFeMnNi@CFP electrocatalyst has demonstrated its promising ability as well as room for improvement in water splitting applications.

References

1. Zhang, D., Zhao, H., Wu, X., Deng, Y., Wang, Z., Han, Y., Li, H., Shi, Y., Chen, X., Li, S., Lai, J., Huang, B., Wang, L., Multi-Site Electrocatalysts Boost pH-Universal Nitrogen Reduction by High-Entropy Alloys. *Adv. Funct. Mater.* **2021**, 31, 2006939
2. Chen, P.-C.; Liu, G.; Zhou, Y.; Brown, K. A.; Chernyak, N.; Hedrick, J. L.; He, S.; Xie, Z.; Lin, Q.-Y.; Dravid, V. P.; O'Neill-Slawecki, S. A.; Mirkin, C. A., Tip-Directed Synthesis of Multimetallic Nanoparticles. *Journal of the American Chemical Society* **2015,** *137* (28), 9167-9173.
3. Kwon, S. G.; Krylova, G.; Phillips, P. J.; Klie, R. F.; Chattopadhyay, S.; Shibata, T.; Bunel, E. E.; Liu, Y.; Prakapenka, V. B.; Lee, B.; Shevchenko, E. V., Heterogeneous nucleation and shape transformation of multicomponent metallic nanostructures. *Nature Materials* **2015,** *14* (2), 215-223.
4. Chen, P.-C.; Liu, M.; Du Jingshan, S.; Meckes, B.; Wang, S.; Lin, H.; Dravid Vinayak, P.; Wolverton, C.; Mirkin Chad, A., Interface and heterostructure design in polyelemental nanoparticles. *Science* **2019,** *363* (6430), 959-964.

Chapter 5

Enhancing OER performance by surface modification and multiple growths of high-entropy alloy nanostructures

The high-entropy alloy nanoparticles CoCuFeMnNi@CFP have shown a promising ability in electrocatalysis for energy conversion. Nevertheless, the electrochemical activities can be enhanced further with appropriate treatment and modification. This chapter demonstrates the changes in surface morphology and composition, which result in the improvement of high-entropy alloy CoCuFeMnNi@CFP nanostructures for oxygen evolution reaction after surface modification by laser treatment. The HEAs characterization will be investigated in comparison to energy conversion effectiveness.

5.1. Rapid laser irradiation surface treatment effect on CoCuFeMnNi@CFP high-entropy alloy.

5.1.1. Laser continuous irradiation post-synthesis treatment

The advantage of rapid laser irradiation is multi-functional, which can be utilized for different purposes by adjusting irradiation mode and parameters. The RLI on carbon-fiber papers can make surface modifications in a controlled manner. The process can be done by adjusting the power and focus point, as well as the duration of exposure and the speed of the scan, to create a specific pattern or porous structure on carbon fiber. The resulting porous surface of carbon fiber yield a higher surface area, which is beneficial for the application of catalytic reaction. On the other hand, the intense heat generated by the laser can induce metal oxidation, which possibly increases the rate of oxygen evolution reaction. After completing the synthesis of high-entropy alloy nanoparticles on carbon fiber paper, the sample was again placed in the vacuum chamber, followed by exposure of it to continuous laser irradiation, with a scanning speed range from 200 to 1000 mm/s and other parameters specified in **Table 5.1**.

Table 5.1: Parameters of laser continuous irradiation for post-synthesis treatment.

Power (W)	Speed (mm/s)	Frequency (kHz)	Pulse width (ns)	Line space (mm)	Spot size (mm)
1 - 8	200 - 1000	Continuous		0.03	0.03

Figure 5.1 shows the porous nanostructure which appeared on the surface of the carbon fiber. Compare to the pristine carbon fiber surface demonstrated in the previous chapter, porous nanostructures provide a higher surface area that allows more efficient chemical and electrochemical reaction. Furthermore, mechanical strength was also increased, granting better support for energy dissipation while growing high-entropy alloy nanoparticles.

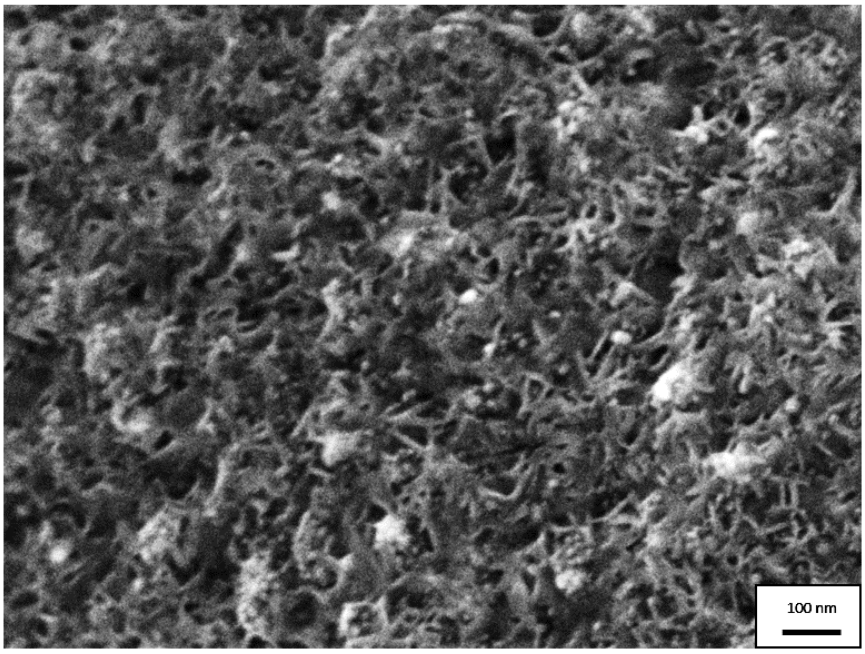

Figure 5.1: FESEM images of porous nanostructure after laser heat treatment

5.1.2. Defect-rich CoCuFeMnNi@CFP high-entropy alloy nanostructures.

Crystallography of the HEAs after laser treatment was studied using high-resolution transmission electron microscopy (HRTEM). **Figure 5.2a** and **5.2b** show bright-field images of some chosen defective regions in the HEAs crystal lattice. The red arrows indicate the nanoscale holes and strained fringes appeared across the HEAs, which are created by the photoexcitation energy that is released during strong laser-material interaction. The square marked area is displayed in **Figure 5.2c** with an inset of the diffraction pattern generated by FFT illustrating the view in {1 1 1} crystal planes. In face-centered-cubic structure, the {1 1 1} crystal planes have the highest atom density and the largest surface energy. As a result, atoms are most likely to be added or removed during the growth or treatment processes, leading to the formation of defects. Figure 5.2d-f show more evidence of the lattice distortion, stacking faults, and dislocations along the (2 -2 0), (0 2 -2), and (2 0 -2) lattice planes, respectively.

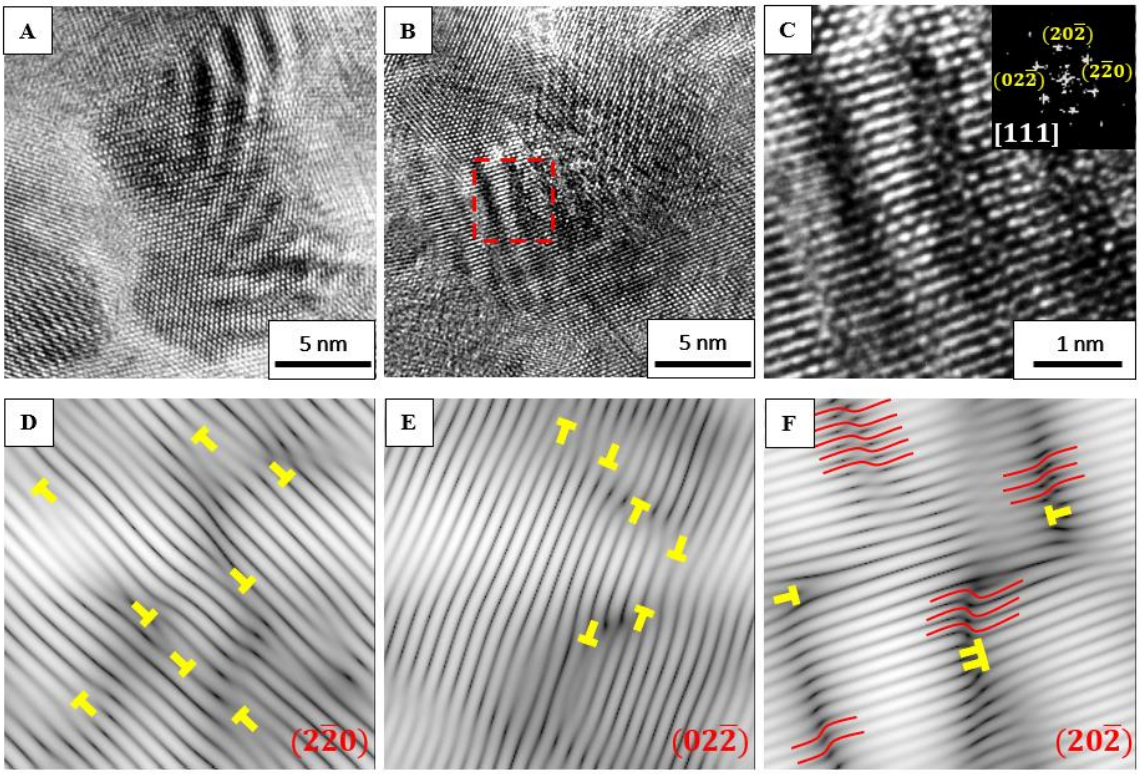

Figure 5.2: (a-b) HRTEM images of typical lattice defect region after laser heat treatment, (c) Zoom-in image of the red marked area in B and its FFT diffraction pattern (inset), (d-f) Inverse FFT image of lattice structure along (2 -2 0), (0 2 -2), and (2 0 -2) respectively.

Together with the porous nanostructure, multi holes and defects were found to be the result of laser irradiation post-synthesis treatment. The vacancies and nanoscale holes can increase the surface energy since they disrupt the regular arrangement of atoms on the surface, creating additional active sites on the surface or building up the surface areato volume-ratio, which can promote electrochemical reactions. However, some defects as dislocations or grain boundaries can act as traps for adsorbed species or intermediates, making the surface less reactive. Therefore, optimization of the parameters used for laser treatments should be investigated, which will be demonstrated in the later section of this chapter.

5.2. Multiple growths of CoCuFeMnNi@CFP high-entropy alloy nanostructures.

The previous chapter has demonstrated the synthesis of CoCuFeMnNi@CFP high-entropy alloy nanoparticles, which will be informed as single growth (SG) from this section onward. The laser irradiation treatment after the first synthesis results not only in defect-rich HEA nanostructures but also enable more surface area through the appearance of the porous nanostructure on the carbon fiber surface. Therefore, repeating the 2 mM nanoparticles synthesis process after laser heat treatment, which resulted in the multiple growths of HEA nanostructures, would be a suitable option to increase the density of nanoparticles and further enhance the electrocatalytic activity. **Figure 5.3** demonstrates the schematic diagram of multiple growt process of HEA nanostructures.

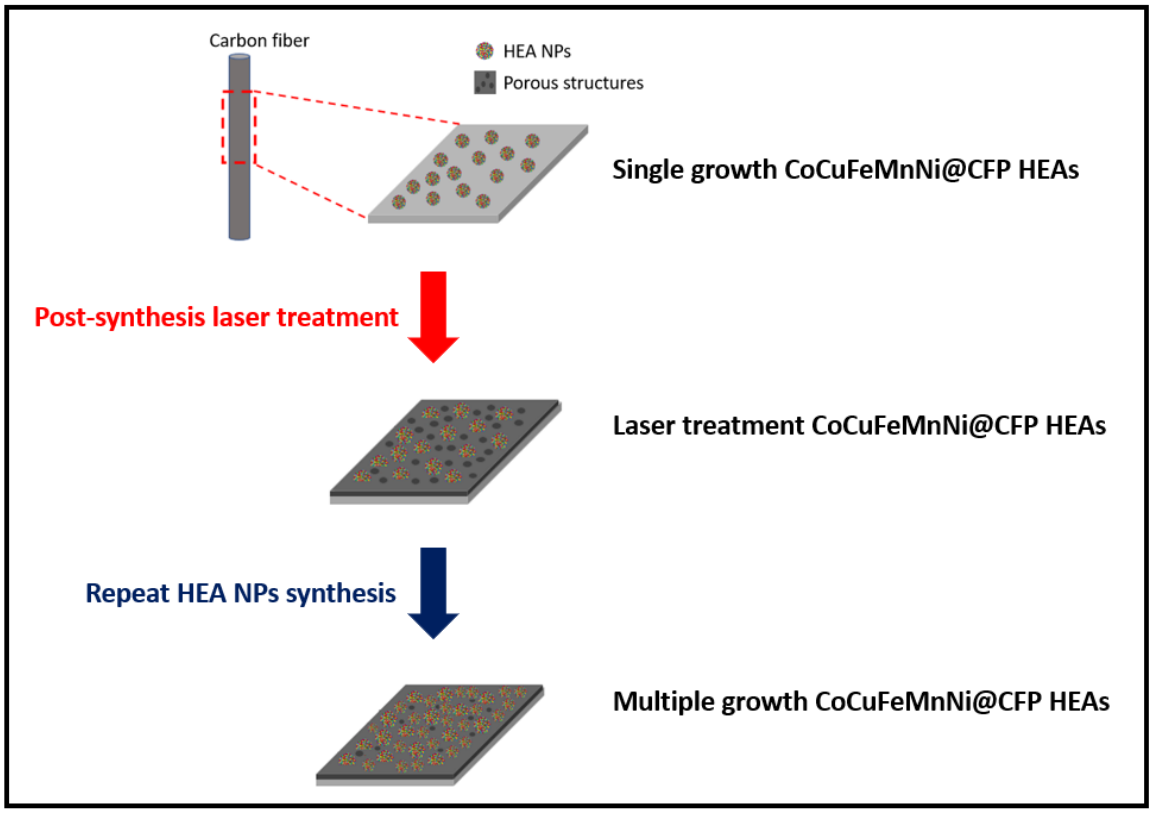

Figure 5.3: Schematic diagram of Multiple growth CoCuFeMnNi@CFP HEA nanostructures process.

5.2.1. Morphology of multiple growth CoCuFeMnNi@CFP HEA nanostructures.

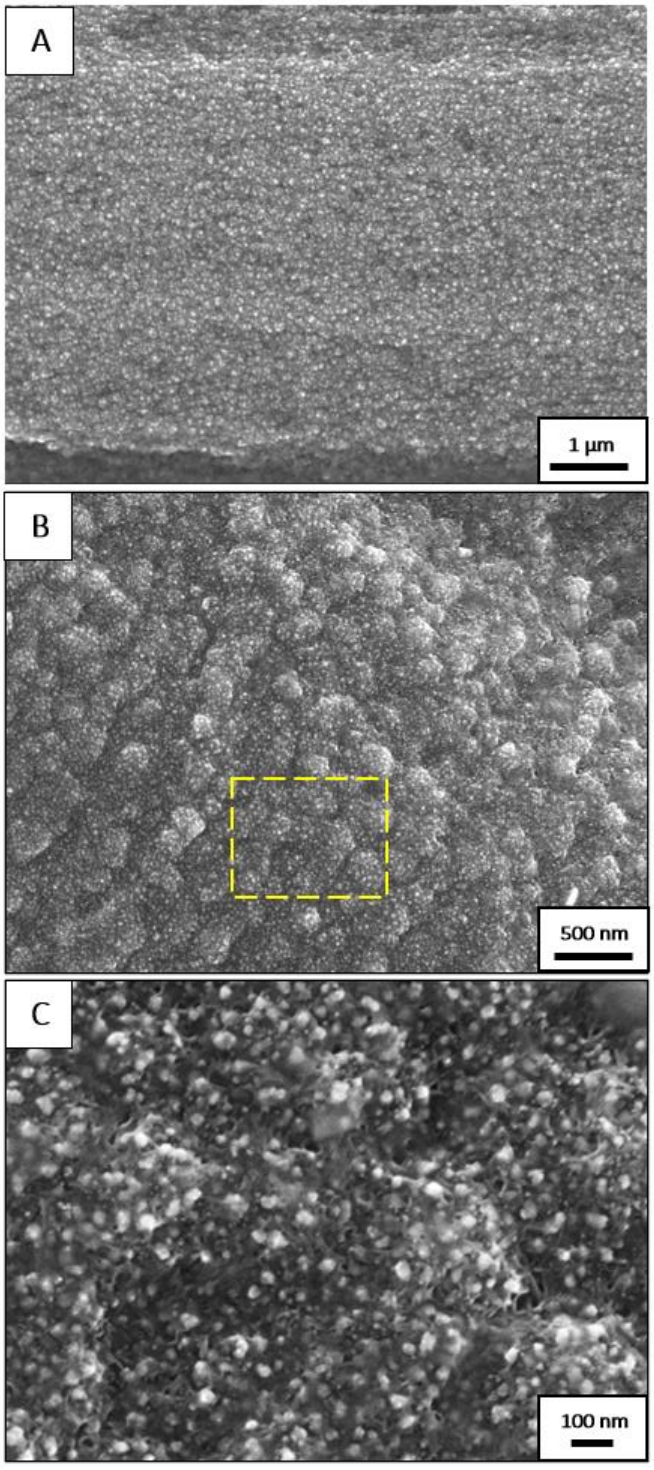

Figure 5.4: Morphology of multiple growth CoCuFeMnNi@CFP HEAs nanostructures
(a) Low magnification FESEM image on the surface of carbon fiber, (b) multiple growths of HEAs nanoparticles on porous nanostructure surface, (c) High magnification image of the marked area.

Figure 5.4 shows the morphology of multiple growths of CoCuFeMnNi@CFP high-entropy alloy nanostructures. The surface of the carbon fiber after fabrication is shown in **Figure 5.4a**. The porous structure formed after laser treatment provide a larger surface area with better support in which more nanoparticles can grow. It also prevented the merging or aggregation of nanoparticles throughout the overlapping growth process. The multiple growths still generate small nanoparticles as same as the single growth of the 2 mM process with an average diameter of 13.32 ± 1.83 nm. A much higher particle density can be observed in **Figure 5.4b-c**, approximately 660 ptcs/μm^2. The particle size distribution plot is illustrated in **Figure 5.5**. The multiple-growth final sample increased the particle density as well as surface area compared to the pristine carbon fiber or the single growth, which will be expected to enhance electrochemical activity.

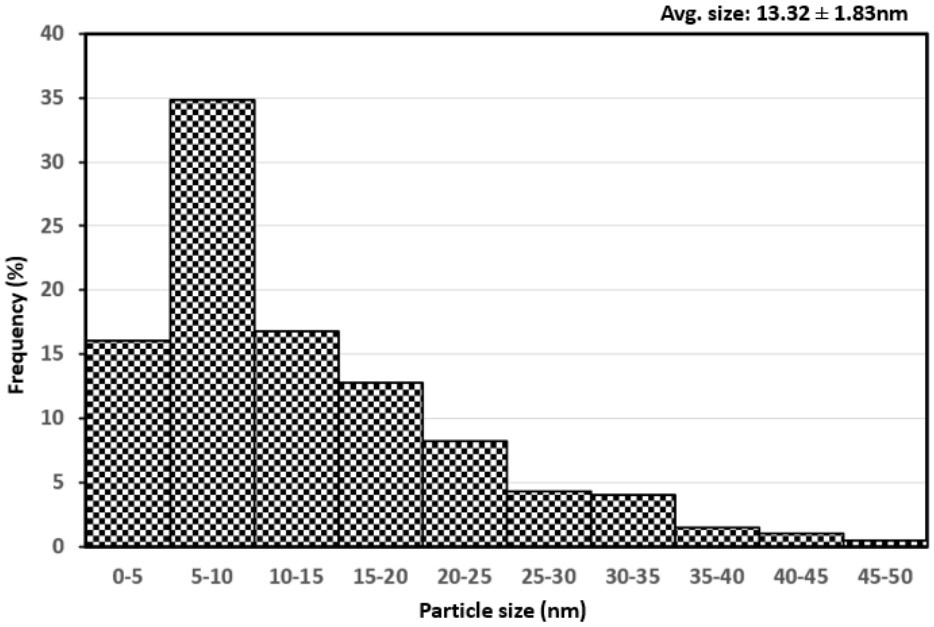

Figure 5.5: Particle size distribution of multiple growths of CoCuFeMnNi@CFP HEAs.

5.2.2. Crystallography of multiple growth CoCuFeMnNi@CFP HEA nanostructures.

Figure 5.6 demonstrates the X-ray diffraction pattern of the multiple growth CoCuFeMnNi@CFP HEAs after laser treatment. Excluding the carbon peak at 54.5° (green), the multiple growth sample maintained two diffraction peaks at 2-theta equals 43.25° and 74.05° (red), which correspond to (111) and (220) crystal planes of a single-phase face-centered cubic lattice structure. In comparison with the XRD result of single growth HEA, the peak of multiple growth HEA is sharper with increased intensity, which indicates slightly larger in size and higher crystallinity HEA NPs have been formed after laser treatment. Besides, additional peaks can be found at 36.60° and 62.85° (black) in the XRD pattern also suggesting the presence of the high-entropy oxides family, which correspond to (311) and (440) crystal planes (JCPDS No. 04-019-3857). The metal-oxides formation is likely to be the consequence of intense heat generated by the post-synthesis treatment.

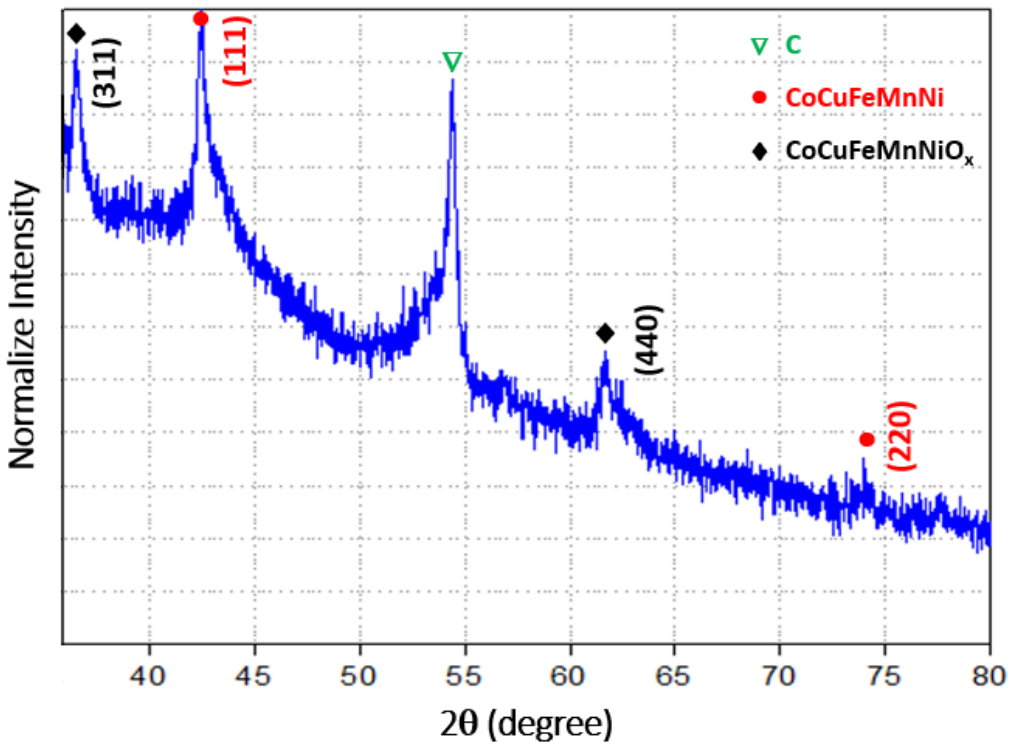

Figure 5.6: X-ray diffraction pattern of multiple growth CoCuFeMnNi@CFP HEAs nanostructures

Figure 5.7 shows the HRTEM image of the sample along with the structure, crystal planes, and the lattice spacing was measured by processing fast Fourier transformation (FFT). As observable in bright-field HRTEM image (**Figure 5.7a)**, HEA nanoparticles, appeared as dark round-like shapes, tightly dispersed across an area of carbon fiber. **Figure 5.7b** shows a high magnification image of a well-oriented representative HEA NPs. Reciprocal spot produced by FFT (inset of **Figure 5.7b)** represents the diffraction pattern along the [1 1 0] axis. Crystalline lattice with no dislocations is proved by inverse FFT images in **Figure 5.7c-e**. The d-spacing is calculated as 1.39 Å in both (-1 1 1) and (-1 1 -1) crystal planes, while the (0 0 -2) d-spacing is 1.23 Å. The crystallography results confirmed FCC crystal structures, and the feasibility of the growth of HEA nanoparticles on porous nanostructures by laser irradiation.

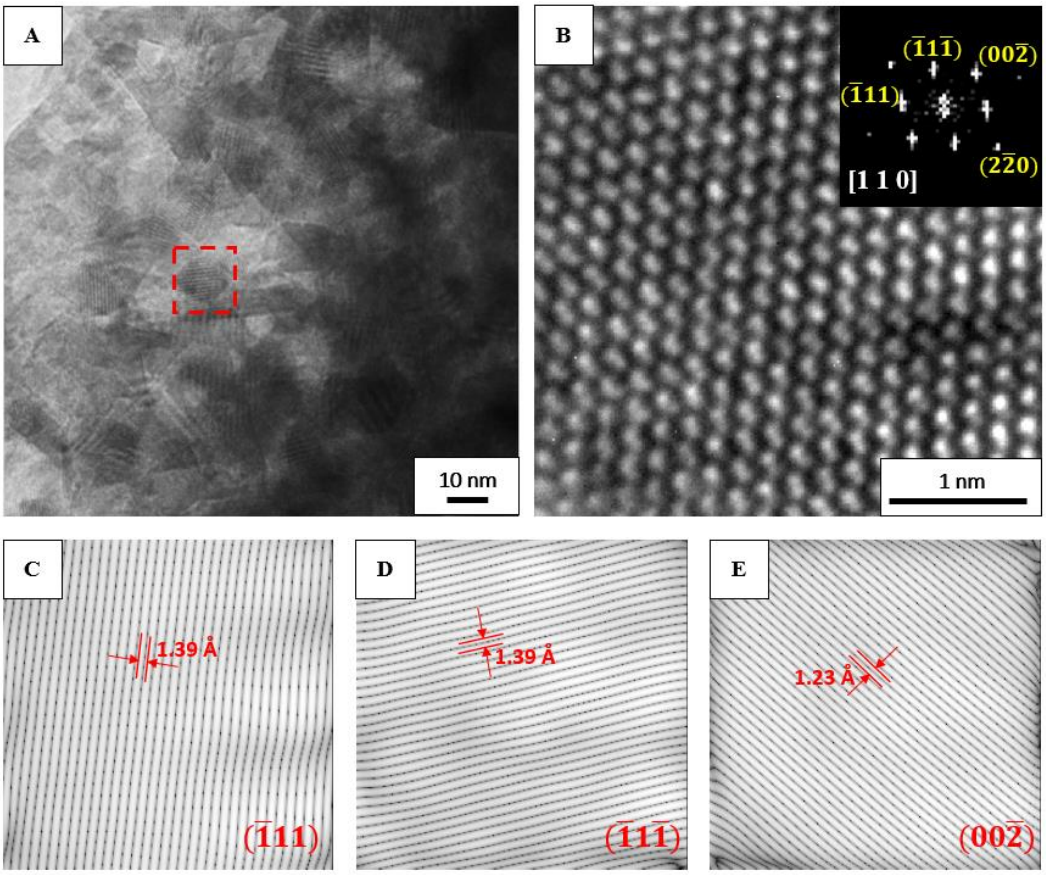

Figure 5.6: (a) low magnification bright-field HRTEM image, (b) high magnification image of the marked area in A and FFT pattern (inset), (c-e) IFFT transformed images along (-1 1 1), (-1 1 -1), and (0 0 -2) lattice planes, respectively of multiple growth HEAs.

5.3. Enhancing Oxygen Evolution Reaction Performance

5.3.1. The effect of laser continuous irradiation post-synthesis treatment on CoCuFeMnNi@CFP high-entropy alloy electrocatalysts

Prior to enhancing the electrocatalytic performance by post-synthesis treatment, the laser continuous irradiation effect on carbon fiber paper-based high-entropy alloys have been studied. **Figure 5.8** shows the linear sweep voltammetry (LSV) of OER electrochemical tests in the potential range of 1.1 to 1.7 V versus RHE through a standard three-electrode system with the scanning rate set to 5 mV/s from an external voltage range of 0 to 0.7 V with a potential step of 0.00244 V. Oxygen evolution reactions were conducted in 1 M KOH electrolyte. The fabricated CoCuFeMnNi@CFP HEAs single growth before treatment (labeled as SG) samples have been compared with the post-synthesis treatment samples by different irradiation speeds (200 mm/s, 400 mm/s, and 800 mm/s), which is inverse proportion with exposure time. The effect of laser power has also been studied by repeating the tests at different laser output powers of 1 W, 2 W, 4 W, and 8 W. At the lowest output power as 1 W, there are slight improvements in OER catalytic performance, which overpotential at a current density of 10 $mA.cm^{-2}$ gradually increased as the inverse proportion of irradiation speed (**Figure 5.8a**), reached 313 mV by irradiation speed of 200 mm/s. **Figure 5.8b-c** show the OER performance at 2 W and 4 W, which the best overpotential at a current density of 10 $mA.cm^{-2}$ is 33 mV higher (297 mV) than the SG before treatment reference sample (330 mV), by irradiating at 2 W with a speed of 400 mm/s. On the other hand, laser treatment at a high power of 8 W results in vast changes as shown in **Figure 5.8d**. Long exposure time at high laser power may damage the carbon fiber substrate, which causes a major drop in electrocatalytic performance.

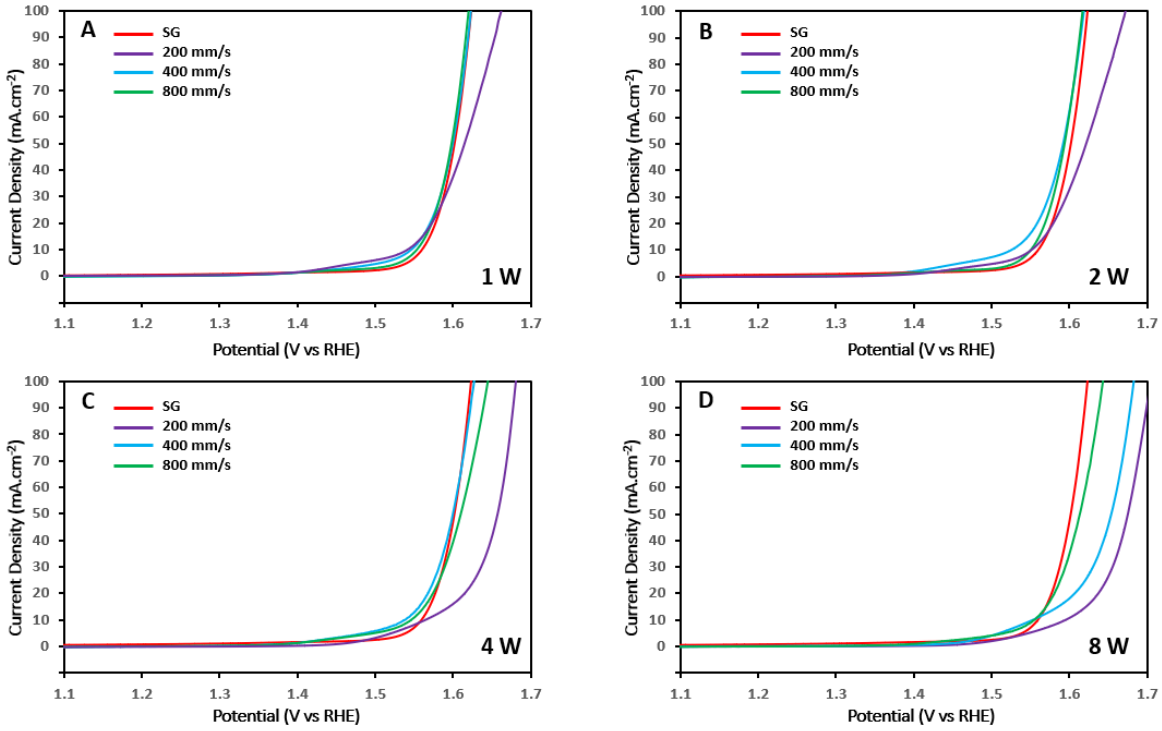

Figure 5.8: LSV curves of OER of CoCuFeMnNi@CFP HEAs before (SG) and after laser continuous irradiation treatment with various irradiation speeds at different laser power (a) 1W, (b) 2W, (c) 4W, and (d) 8W.

The relative effect of laser irradiation power speed to the overpotential at the current density of 10 mA.cm^{-2} is shown in **Figure 5.9**. The overpotential of a single growth sample before laser treatment is displayed as a horizontal red line at 330 mV. Very fast irradiation (800 mm/s) caused a marginal difference in the catalytic activity despite the laser power because the exposure time is not long enough to make significant modifications on the surface of carbon fiber or the HEA NPs. The irradiation speed of 400 mm/s quantitatively makes the most efficient treatment to enhance the OER catalytic activity of the CoCuFeMnNi@CFP high-entropy alloy electrocatalysts.

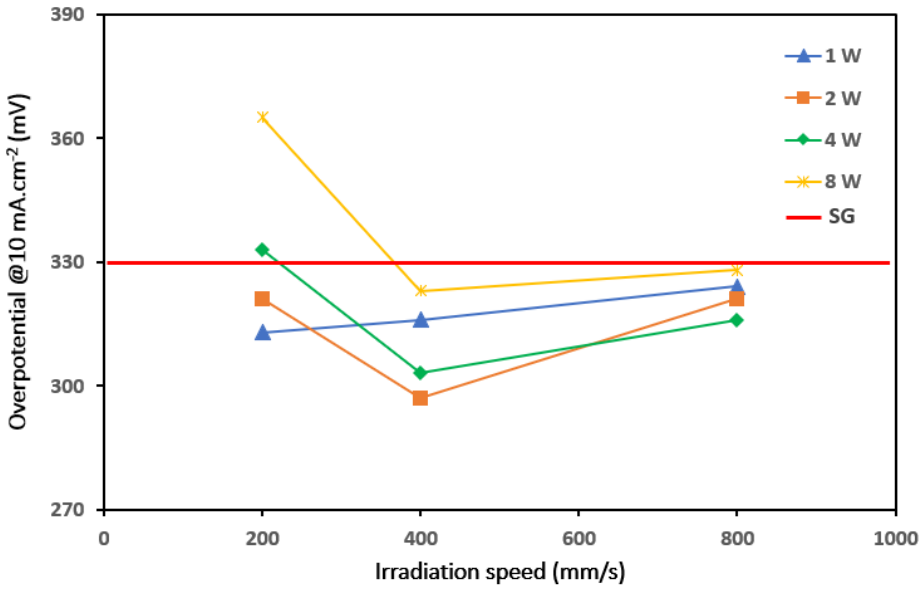

Figure 5.9: OER overpotential comparison of different laser irradiation power and speed.

5.3.2. Enhancing OER performance by multiple growths of CoCuFeMnNi@CFP high-entropy alloy nanostructures

Figure 5.10 shows the electrochemical tests of the fabricated and enhanced CoCuFeMnNi@CFP HEA electrocatalysts and the comparison between the single growth (SG-CoCuFeMnNi@CFP), the laser treatment (LT-CoCuFeMnNi@CFP), and the multiple growths of (MG-CoCuFeMnNi@CFP) samples. Oxygen evolution reactions were conducted in 1 M KOH electrolyte through a standard three-electrode system with the scanning rate set to 5 mV/s from an external voltage range of 0 to 0.7 V with a potential step of 0.00244 V. The data was converted and plotted as current density to potential versus RHE. **Figure 5.10a** demonstrates the LSV curves catalytic activities for the OER of the three mentioned samples. The results show the improvement of the multiple growths in comparison to the original single growth of HEA nanoparticles and the post-synthesis treatment sample. The MG sample reached the ideal overpotential of 276 mV at a current density of 10 $mAcm^{-2}$ as shown in **Figure 5.10b**, which is 21 mV lower than the LT sample (297 mV) and 54 mV lower than the original SG HEA NPs electrocatalyst (330 mV).

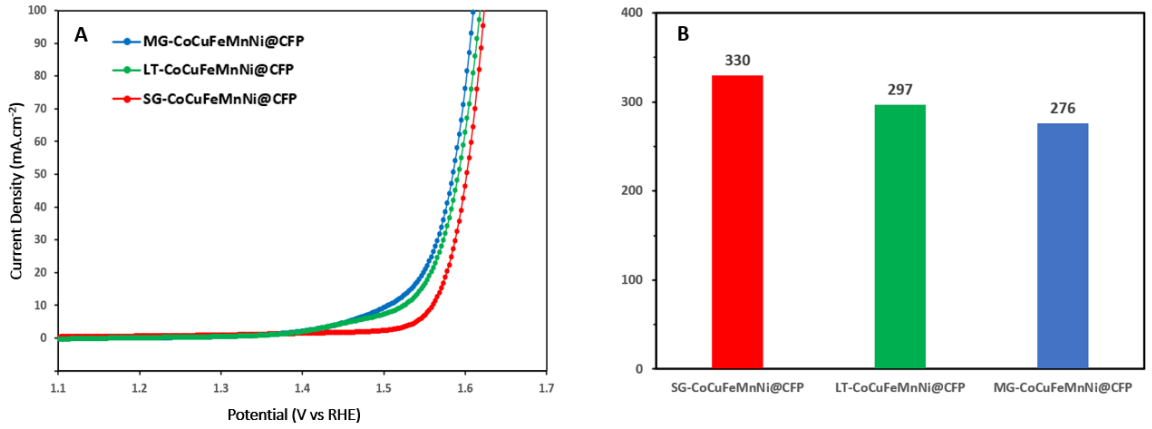

Figure 5.10: Electrochemical test of the single growth (SG), laser treatment (LT), and multiple growths (MG) of CoCuFeMnNi@CFP high-entropy alloy nanostructures: a) LSV curve, b) Overpotential at a current density of 10 $mA.cm^{-2}$

Figure 5.11 illustrates the cyclic voltammetry (CV) results of SG-HEAs and MG-HEAs. The inset image shows the CV test in OER region of 1.1 to 1.8 V vs RHE. It is wise to suspect the oxidation of transition metals. From the CV results, the catalytic activity of the MG-HEAs sample was improved in comparison to the SG-HEAs sample in both the oxidation and reduction paths.

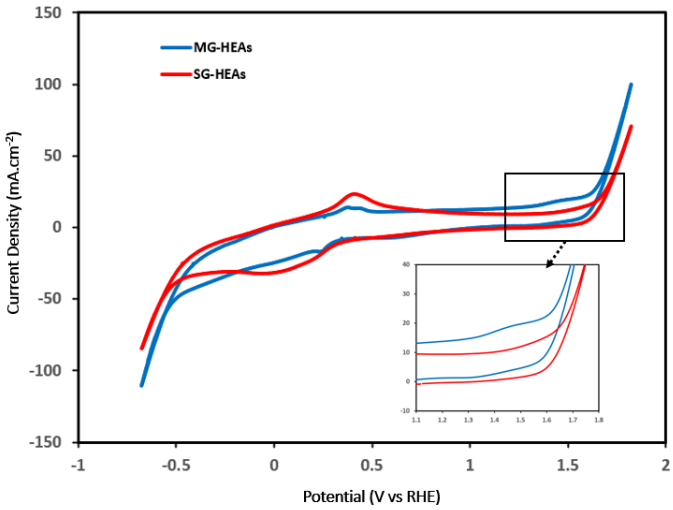

Figure 5.11: CV test result of the single growth (SG) and multiple growths (MG) of CoCuFeMnNi@CFP high-entropy alloy nanostructures. (Inset: enlarged image in OER range 1.1 V to 1.8V)

Figure 5.12a shows the Tafel slopes of SG, LT, and MG CoCuFeMnNi HEAs are 64.1, 68.7, and 79.6 $mVdec^{-1}$, respectively. The multiple growth CoCuFeMnNi HEA nanostructures exhibited the least Tafel slope that less overpotential is required to achieve a specific current density level, which agreed with the dominant OER performance as compared to other samples. **Figure 5.12b** displayed the electrochemical impedance spectroscopy (EIS) plot performed at the operating voltage of 1.55 V vs. RHE with the SRC equivalent circuit (**Figure 5.12b** inset) was simulated and fitted by NOVA software. MG sample presented the smallest semicircle with charge transfer resistance R_{ct} value of 4.9 Ω compared to 9.2 Ω of the laser treatment sample and 25.8 Ω of the single growths of catalysts. The incredibly low charge transfer resistance of multiple growth catalyst might be due to the formation of oxides (*O) at the active site on the surface of the HEA after treatment as being exposed to the laser.

The free energy mechanism suggested the reaction process begins with the formation of *OH and *O intermediates. After that, on the surface of the active site is expected to form superoxide intermediates (*OOH) due to OH^- absorption, which is further formed an O-O bond by couple-electron transfer. The O-O bond formation will be released as O_2 and leave the active site (*) clear for the next oxygen evolution reaction.[1-3] Furthermore, the difference adsorption energy between *OOH and *OH ($\Delta G_{OH} - \Delta G_{OOH}$) is constant at 3.1 eV. Therefore, the formation of microsite defects and oxide species in the multiple growth HEA sample would benefit and optimize the energy level of *O, which resulted in the $\Delta G_{OH} - \Delta G_{O}$ and $\Delta G_{O} - \Delta G_{OOH}$ as close as 1.6 eV for rapid electron transfer at the catalyst and electrolyte interface in the most considerable multiple step reaction process.[12]

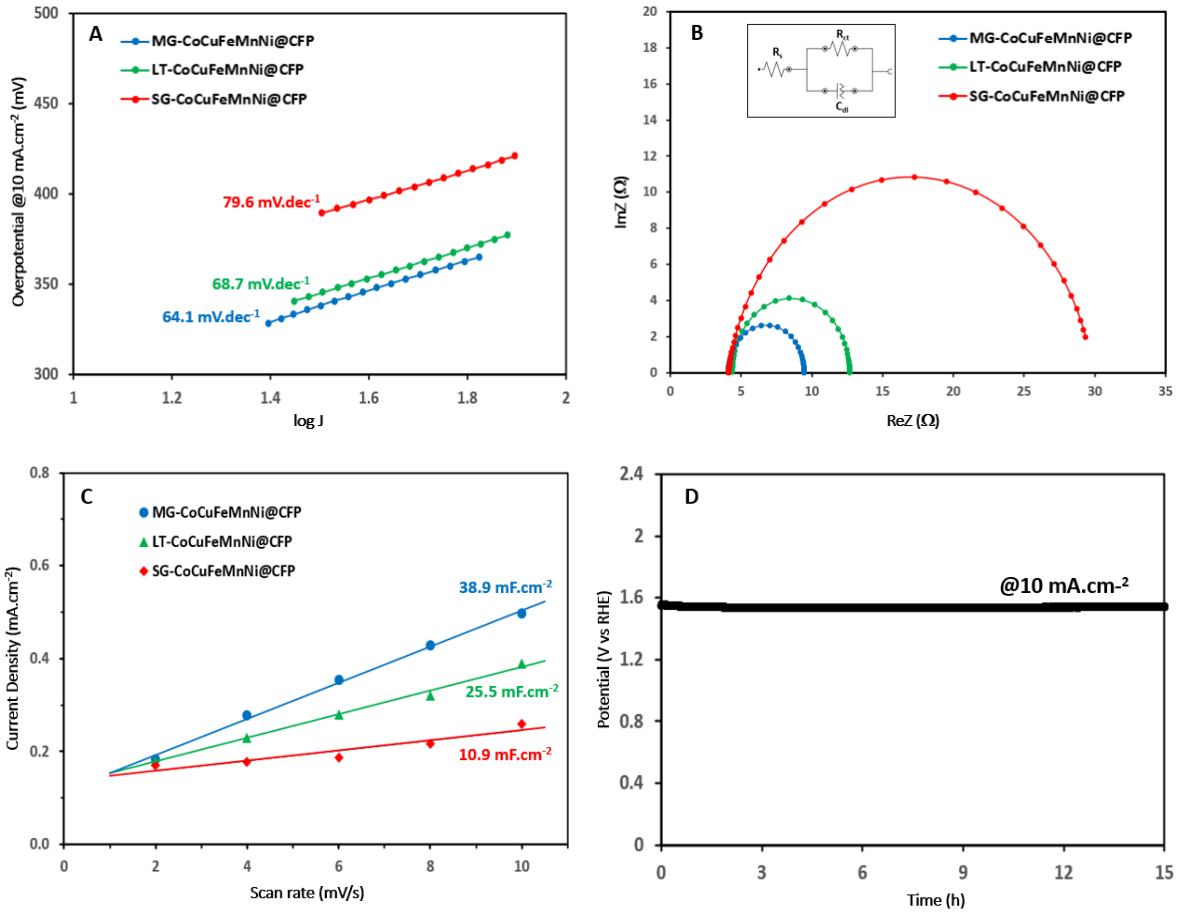

Figure 5.12: a) Tafel plot, b) EIS plot with equivalent circuit (inset), (c) C_{dl} capacitance, and (d) Chronoamperometry stability test for multiple growths of CoCuFeMnNi high-entropy alloy nanostructures.

In addition, the electrochemical active surface area (ECSA) was investigated through the double-layer capacitance measured in the capacitive region, where the current is relatively small and determined primarily by the charging and discharging of the electric double-layer at the electrode-electrolyte interface. The slope of this linear region is equal to the double-layer capacitance (C_{dl}). The values of C_{dl} were fitted as 38.9 mF.cm^{-2}, 25.5 mFcm^{-2}, and 10.9 mF.cm^{-2} respectively of MG, LT, and SG HEA nanostructures electrocatalysts as shown in **Figure 5.12c**. Thus, the ECSA values are calculated to correspond to 972.5 cm^{-2}, 637.5 cm^{-2}, and 272.5 cm^{-2}. The MG HEA sample exhibited the highest ECSA value due to the larger surface area caused by laser treatment, as well as well dispersed HEA nanoparticles provided sufficient reactive sites.

The best OER performance of MG HEA sample was selected to study its stability, which is demonstrated in **Figure 5.12d**, by several chronoamperometry tests at 1.55 V vs. RHE for 12 hours. After 12 hours of stability test, the MG HEA sample remained at over 92% current retention and almost no materials degradation.

Recently reported OER performance of high-entropy materials catalysts are displayed in **Table 5.2**. The MG-CoCuFeMnNi@CFP HEAs in this work are the most competitive electrocatalyst compared to others. Besides, laser irradiation appeared to be the fastest and simple method relatively with mechanical alloying, induction melting, solvothermal, or eutectic approaches.

Table 5.2: OER performance comparison of MG-CoCuFeMnNi@CFP electrocatalyst with recently reported HEA catalysts.

Catalysts	**Electrolyte**	**η10 (mV)**	**Tafel slope ($mVdec^{-1}$)**	**Ref.**
MnFeCoNi	1 M KOH	302	83.7	[4]
FeCoNiCuZn	1 M KOH	340	48	[5]
CoFeLaNiPt	0.1 M KOH	377	150	[6]
AlCrFeNiCu	1 M KOH	270	77.5	[7]
FeCoNiCrNb	0.1 M KOH	288	27.7	[8]
CoCuFeMnNiO	1 M KOH	350	76.7	[9]
CoNiMnZnFeO	1 M KOH	336	47.5	[10]
CoCrFeMnNiP	1 M KOH	320	60.8	[11]
Multiple growth CoCuFeMnNi@CFP	**1 M KOH**	**276**	**64.1**	**This work**

5.4. Conclusions

The proper use of laser irradiation is an effective way to introduce surface modification on highly crystalline CoCuFeMnNi@CFP high-entropy alloy nanostructures electrocatalysts. By controlling the power and speed of the laser, the porous nanostructures were created on the surface of the carbon fiber that increase the surface area. Simultaneously, the high energy of the laser beam causes a chain of events that creates multiple defects in the HEA nanoparticles. The combination of crystal structure defects with porous nanostructures produces additional active sites on the surface and increases the surface area-to-volume-ratio, which leads to enhanced performance in electrocatalytic reactions. The vacancies formed after laser treatment act as active sites for absorbing water molecules. Besides, the metal active sites can further polarize the H_2O molecules, which longer the distance between oxygen and hydrogen atoms in the O-H bond, causing lower activation energy for the oxygen evolution reaction. The additional layer of HEA nanoparticles grown on the porous nanostructure doubles the nanoparticle density on the carbon fiber surface, which enlarges the surface-to-volume ratio and further increases the OER performance.

References

1. Sharma, L.; Katiyar, N. K.; Parui, A.; Das, R.; Kumar, R.; Tiwary, C. S.; Singh, A. K.; Halder, A.; Biswas, K., Low-cost high entropy alloy (HEA) for high-efficiency oxygen evolution reaction (OER). *Nano Research* **2021**.
2. Waag, F.; Li, Y.; Ziefuß, A. R.; Bertin, E.; Kamp, M.; Duppel, V.; Marzun, G.; Kienle, L.; Barcikowski, S.; Gökce, B., Kinetically-controlled laser-synthesis of colloidal high-entropy alloy nanoparticles. *RSC Advances* **2019,** *9* (32), 18547-18558.
3. Ma, Y.; Ma, Y.; Wang, Q.; Schweidler, S.; Botros, M.; Fu, T.; Hahn, H.; Brezesinski, T.; Breitung, B., High-entropy energy materials: challenges and new opportunities. *Energy & Environmental Science* **2021,** *14* (5), 2883-2905.
4. Dai, W.; Lu, T.; Pan, Y., Novel and promising electrocatalyst for oxygen evolution reaction based on MnFeCoNi high entropy alloy. *Journal of Power Sources* **2019,** *430*, 104-111.
5. Huang, J.; Wang, P.; Li, P.; Yin, H.; Wang, D., Regulating electrolytic Fe0.5CoNiCuZnx high entropy alloy electrodes for oxygen evolution reactions in alkaline solution. *Journal of Materials Science & Technology* **2021,** *93*, 110-118.
6. Glasscott, M. W.; Pendergast, A. D.; Goines, S.; Bishop, A. R.; Hoang, A. T.; Renault, C.; Dick, J. E., Electrosynthesis of high entropymetallic glass nanoparticles for designer, multi-functional electrocatalysis. *Nat Commun* **2019,** *10* (1), 2650.
7. LH Liu, N. L., Mei Han, JR Han, HY Liang, Scalable synthesis of nanoporous high-entropy alloys for electrocatalytic oxygen evolution. *Rare Metals* **2021**.
8. Ding, Z.; Bian, J.; Shuang, S.; Liu, X.; Hu, Y.; Sun, C.; Yang, Y., High Entropy Intermetallic–Oxide Core–Shell Nanostructure as Superb Oxygen Evolution Reaction Catalyst. *Advanced Sustainable Systems* **2020,** *4* (5), 1900105.
9. Wang, D.; Liu, Z.; Du, S.; Zhang, Y.; Li, H.; Xiao, Z.; Chen, W.; Chen, R.; Wang, Y.; Zou, Y.; Wang, S., Low-temperature synthesis of small-sized high entropyoxides for water oxidation. *Journal of Materials Chemistry A* **2019,** *7* (42), 24211-24216.

10. Zhang, Y.; Dai, W.; Zhang, P.; Lu, T.; Pan, Y., In-situ electrochemical tuning of (CoNiMnZnFe)3O3.2 high entropyoxide for efficient oxygen evolution reactions. *Journal of Alloys and Compounds* **2021,** *868*, 159064.
11. Zhao, X.; Xue, Z.; Chen, W.; Wang, Y.; Mu, T., Eutectic Synthesis of High entropyMetal Phosphides for Electrocatalytic Water Splitting. *ChemSusChem* **2020,** *13* (8), 2038-2042.
12. Yu, Z. Y., Duan, Y., Feng, X. Y., Yu, X., Gao, M. R., & Yu, S. H. (2021). Clean and Affordable Hydrogen Fuel from Alkaline Water Splitting: Past, Recent Progress, and Future Prospects. *Advanced Materials* **2021**, *33(31)*

Chapter 6

Conclusions and Recommendations

This chapter concludes and discusses the threads of the thesis. The summary including physical and electrochemical properties of high-entropy alloys electrocatalysts will be discussed. Commercial viability and potential challenges for future industrial applications will be addressed. The reconnaissance studies the effect of laser parameters on lattice structure manipulations that does not warrant a complete chapter. The opportunities and strategies for future work are proposed based on the current research in this thesis.

6.1. General Discussion

The electrochemical properties of high-entropy alloys and the need to replace noble metals have marvelously promoted the research for abundant metal catalysts that exhibit high efficiency in energy conversion and storage. This project directs attention to taking advantage of near infra-red 1064 nm laser irradiation to:
(1) Fabricate the high-entropy alloy nanoparticles on carbon fiber electrode for electrocatalysis,
(2) Produce surface modification to enhance the electrocatalytic capabilities through post-synthesis treatment,
(3) Synthesis of multiple growth CoCuFeMnNi@CFP HEA nanostructures advanced in oxygen evolution reaction.

One of the primary advantages of utilizing abundant metals in HEAs is the cost-effectiveness they bring to electrocatalysis. Abundant metals are readily available and have lower market prices compared to their precious counterparts, ensuring a cost-effective production process. This significantly reduces the overall manufacturing cost and makes HEAs more accessible for large-scale industrial applications. Additionally, the sustainable and scalable supply chain of abundant metals ensures a stable and reliable source, eliminating concerns related to resource scarcity and cost volatility.

Although laser-assisted synthesis has shown significant promise for producing HEA nanostructures, there are various limitations and challenges to be overcome as the method is scaled up for industrial applications. One of the primary challenges is that the larger processing area will require longer processing time, which will lead to high energy consumption. Therefore, the key is to increase efficiency to adapt to various industry demands. Micro-lens arrays, spatial light modulators should be investigated as versatile solutions for further modification and adaptation to the laser irradiation process. Another limitation is the heat-affected area during laser synthesis, which is regulated by laser intensity and sample positioning. The uniform heating distribution and precise control of laser parameters across higher manufacturing scales become progressively complex, which

will affect the synthesis yield and reproducibility of HEA electrocatalysts in conventional production.

The rapid laser irradiation process has shown the feasibility of fabricating high-performance HEA electrocatalysts for OER. **Table 6.1** summarize the results of this work with the relative factors involved in the investigation. Energy conversion efficiency and stability have always been important factors to bring HEA up to compare with other conventional alloys. The high number of elements greatly increases the configurational entropy, which leads to phase stability by decreasing Gibb free energy.[1] Thus, understanding the capabilities of NIR laser irradiation towards materials engineering will provide useful insights into building a conventional model of HEA catalysts for various academic and industrial applications.

Table 6.1: Summary and comparison of the works.

<table>
<tr><th></th><th colspan="3">CoCuFeMnNi@CFP nanoparticles</th><th colspan="4">Post-synthesis laser treatment</th><th>Multiple growth CoCuFeMnNi@CFP HEAs</th></tr>
<tr><td>Methods</td><td colspan="3">Rapid pulsed laser irradiation</td><td colspan="4">Rapid continuous laser irradiation</td><td>Pulsed + Continuous laser irradiation</td></tr>
<tr><td>Targets</td><td colspan="3">HEA nanoparticles</td><td colspan="4">Surface modifications (porous nanostructure, vacancy defects)</td><td>HEA nanostructures</td></tr>
<tr><td rowspan="4">Investigated factors</td><td colspan="3" rowspan="2">Precursor concentration</td><td colspan="4">Speed (mm/s)</td><td rowspan="4">Combined</td></tr>
<tr><td colspan="2">200</td><td>400</td><td>800</td></tr>
<tr><td rowspan="2">2 mM</td><td rowspan="2">5 mM</td><td rowspan="2">10 mM</td><td colspan="4">Power (W)</td></tr>
<tr><td>1</td><td>2</td><td>4</td><td>8</td></tr>
<tr><td>Featured nanoparticles diameter</td><td>~10 nm</td><td>~20 nm</td><td>~150 nm</td><td colspan="4">10 – 20 nm</td><td>~10 nm</td></tr>
<tr><td>OER overpotential η10 (mV)</td><td>330</td><td>344</td><td>368</td><td>313</td><td>297</td><td>308</td><td>323</td><td>276</td></tr>
<tr><td>Tafel slope (mVdec^{-1})</td><td colspan="3">79.6</td><td colspan="4">68.7</td><td>64.1</td></tr>
<tr><td>Stability</td><td colspan="8">High stability in alkaline</td></tr>
</table>

6.1.1. Discussion on the synthesis of HEA nanoparticles by laser irradiation

While conventional noble metals and alloy catalysts have been widely used in various energy conversion processes, such as fuel cells and water splitting, the scarcity and cost of these metals limit their commercialization. High-entropy alloys recently attract research attention as catalysts for water splitting applications due to their high chemical stability and tunability composed of multiple elements. It is necessary to compose non-noble metal HEAs catalysts, which yield ideal onset potential as well as great stability and durability in long-term applications. In this work, rapid laser irradiation has proven to be a fast and effective strategy to fabricate CoCuFeMnNi HEA nanoparticles on carbon fiber substrate. The nanoparticle size can be controlled by various parameters to create 10 – 150 nm diameter round-shape particles. The element composition is confirmed by XRD and EDS, forming a single-phase alloy containing five chosen transition metals. The well-oriented face-centered cubic crystal structure can be observed as well as prefer crystalline planes and nanoscale distribution via TEM.

The efficiency and stability of energy conversion have always been crucial factors that have been considered in the comparison of HEAs with other conventional alloys. Various electrochemical tests, including linear sweep voltammetry, cyclic voltammetry, and electrochemical impedance spectroscopy, have been employed to investigate the fabricated CoCuFeMnNi@CFP HEAs electrolysis performance, especially in OER. The results demonstrate comparable or even better electrocatalytic capability when compared to pure noble metal and their alloys, bimetallic, trimetallic alloys, and the other reported composites. The outcome has proven the economic strategy and development of the non-noble metal HEAs are competitive to provide efficient electrocatalysts.

6.1.2. Discussion on the post-synthesis treatment by rapid continuous laser irradiation.

The proper use of laser irradiation is an effective way to introduce surface modification on highly crystalline CoCuFeMnNi@CFP high-entropy alloy nanostructures electrocatalysts. By regulating the intensity and exposure duration of the laser, the porous nanostructures are formed on the surface of the carbon fiber which increases the surface area. The porous structures enlarge the surface area, allowing efficient electrochemical reactions. Besides, the porous surface also acts as a nest for the growth of nanoparticles. At the same time, the high energy of the laser beam triggers a series of events that generate multiple defects in the HEA nanoparticles. The combination of crystal structure defects with porous nanostructures creates additional active sites on the surface and increases the surface area-to-volume ratio, which leads to enhanced performance in electrocatalytic reactions. The parameters used in laser treatments have been investigated and optimized for the best outcome which promotes electrocatalytic performance.

Defects in crystal structures can have a complex effect on electrocatalytic performance. Some dislocations and grain boundaries can act as traps for adsorbed species, which decreases the surface energy and make it less reactive. On the other hand, vacancies or interstitials can increase surface energy since they disrupt the regular arrangement of the lattice, creating more reactive sites. The vacancies formed after laser treatment act as active sites for absorbing water molecules and other intermediates. Besides, the metal active sites can further polarize the H_2O molecules, which longer the distance between oxygen and hydrogen atoms in O-H bond, causing lower activation energy for the oxygen evolution reaction.[3] The formation of high-entropy oxides along with original HEAs was found after the laser treatment. The oxides at the active site fasten the electron transfer while absorbing OH- ions in alkaline media to form O-O bonds through HOO* intermediates, which will be released as O_2.[2] Thus, further enhancing the OER performance.

6.1.3. Discussion on the multiple growths of CoCuFeMnNi@CFP HEA nanostructures.

The CoCuFeMnNi@CFP HEA nanoparticles have demonstrated their promising ability and stability in electrocatalytic. Growing multiple layers of HEA nanoparticles by laser irradiation can create highly active and stable catalysts, while the size and shape of the HEA nanoparticles can be regulated. However, simply growing the nanoparticles could result in the aggregated cluster or the formation of larger nanoparticles, which will eventually reduce the surface area-to-volume ratio and lower the catalytic activities. The development of laser irradiation treatment effect on the fabricated HEA electrocatalysts has given access to layering HEA nanostructure without the mentioned concerns. This work illustrates a combination method to grow addition layers of HEA nanoparticles on the porous nanostructure that multiplied the nanoparticle density on the carbon fiber surface while remains the average particle diameter, which enlarges the surface-to-volume ratio and further increases the OER performance. The results show highly crystalline HEA nanoparticles are able to form on the porous structure, along with the defect-rich HEA nanoparticles generated by laser treatment. The combination of these features greatly enhanced the OER performance, especially lowering the potential required to reach a certain current density, as well as enabling faster electrode-electrolyte charge transfer and enlarging the double-layer capacitance. High stability and durability of the electrocatalysts have also been recorded by chronoamperometry test in alkaline media.

Overall, rapid laser irradiation has proven its feasibility and adaptability in both synthesis and post-synthesis treatment, allowing the multiple growths of the HEA nanostructures, which is commendable to improve the energy conversion effectiveness. It is worth commenting that the multiple growths of earth-abundant HEA electrocatalysts are the potential solution for the commercialization and scaling challenges of conventional noble metal catalysts in energy conversion applications.

6.2. Outstanding Questions

6.2.1. Defects Engineering and Lattice Structure Manipulation by Regulating Parameters of Laser Irradiation

In **chapter 5**, the previous results demonstrated the post-synthesis treatment enhanced the electrocatalytic activities by creating defects and imperfection lattice structures in the HEAs. However, the mechanism of the formation of defects and its effects on surface energy is unclear. DFT calculation and HAADF-STEM simulation can be employed for future investigation, which will provide a systematic understanding of defects engineering by laser irradiation.

Reconnaissance studies have shown that the morphology and structure of the HEA nanoparticles are affected by some laser parameters during the laser irradiation synthesis. **Figure 6.1** show the abnormal morphology of HEAs when irradiated by different laser parameters. Upon low power with a short irradiation time of the laser, the mixed-metal precursor decomposed incompletely, due to lack of thermal energy generated (**Figure 6.1a**). The nanoparticles aggregated or become larger in size as shown in **Figure 6.1b**, because of over-heating due to increasing the duration of laser irradiation. Occasionally, other intermetallic structures have formed under specific laser parameters, like nanosheets (**Figure 6.1c**). Therefore, more research should be the target for future work to investigate the transition of crystal phase and structure under the influence of laser irradiation.

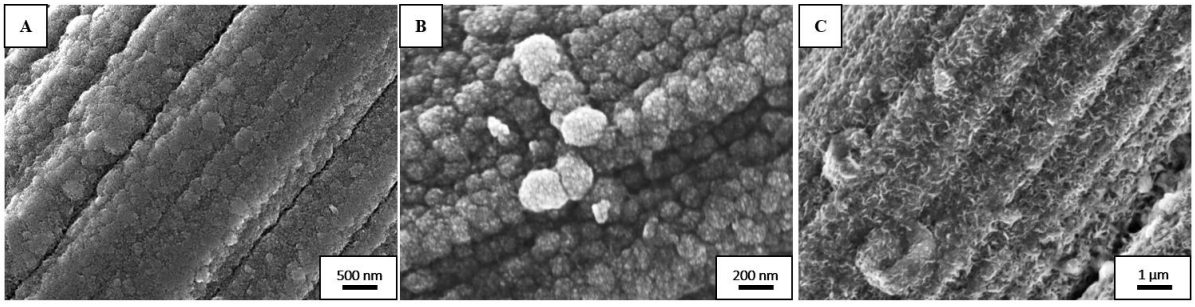

Figure 6.1: FESEM morphology images (a) incomplete decomposition of precursor, (b) aggregated nanoparticles, (c) nanosheets

6.2.2. Bifunctional Electrocatalysts

The laser irradiation on mixed-metal salt precursor allows endless options for the combination of elements in the synthesis of HEAs. As well as selective earth-abundant metals for cost-effective applications, bifunctional electrocatalysts which experienced excellent catalytic activity toward both half-reactions of the water splitting are of great interest. Bifunctional electrocatalysts are materials that can drive both oxygen evolution reaction (OER) and hydrogen evolution reaction (HER) in aqueous electrolytes for various energy conversion and storage applications, such as water splitting, fuel cells, and rechargeable metal-air batteries. The development of highly active and stable bifunctional electrocatalysts is still under significant challenges. Therefore, more research can be focused on improving their performance through laser synthesis strategy and materials design.

6.2.3. Laser-assisted 3D Printing of High-entropy Alloy Electrocatalysts

The effects of laser irradiation on the liquid mixture of metals salt and the carbon substrate to form the second layer of HEAs have been studied in this work. Multiple-layer growth of HEAs is worth investigating as additive manufacturing for electrocatalysts. 3D Printing has the potential to revolutionize the production of electrocatalysts for energy conversion. It allows the rapid and cost-effective production of complex and highly tailored catalysts that greatly improve the efficiency of energy conversion processes.

Future research can focus on utilizing the laser to selectively sinter or grow interlayers of carbon fibers/carbon nanotubes and high-entropy alloys on a conductive base, which eventually builds up a 3D structure. It also allows for the creation of customized electrocatalysts with unique properties, like surface modification and direct laser treatment simultaneously. Thus, promising results are expected for high-performance electrocatalysts by laser-assisted 3D printing, and much attention is required for further research in its application for high-entropy alloys materials.

References

1. Yeh, J. W.; Chen, S. K.; Lin, S. J.; Gan, J. Y.; Chin, T. S.; Shun, T. T.; Tsau, C. H.; Chang, S. Y., Nanostructured High-Entropy Alloys with Multiple Principal Elements: Novel Alloy Design Concepts and Outcomes. *Advanced Engineering Materials* **2004,** *6* (5), 299-303.
2. Sharma, L.; Katiyar, N. K.; Parui, A.; Das, R.; Kumar, R.; Tiwary, C. S.; Singh, A. K.; Halder, A.; Biswas, K., Low-cost high entropy alloy (HEA) for high-efficiency oxygen evolution reaction (OER). *Nano Research* **2021**.
3. Lu, Y., Li, C., Zhang, Y., Cao, X., Xie, G., Wang, M., Peng, D., Huang, K., Zhang, B., Wang, T., Junsheng, W., & Huang, Y., Engineering of cation and anion vacancies in Co3O4 thin nanosheets by laser irradiation for more advancement of oxygen evolution reaction. *Nano Energy* **2021**, *83*, 105800.